Behaviour of fluid-mobile elements across a high-pressure serpentinization front (Monte Maggiore unit, Alpine Corsica)

Behaviour of fluid-mobile elements across a high-pressure serpentinization front (Monte Maggiore unit, Alpine Corsica)

Francesco Ressico [a, *], Enrico Cannaò [b], Orlando Sébastien Olivieri [a], Zeudia Pastore [a, c], Veronica Peverelli [a], Nadia Malaspina [d], Alberto Vitale Brovarone [a, e, f]

[a] Department of Biological, Geological, and Environmental Sciences, Università degli Studi di Bologna, Bologna, Italy.

[b] Dipartimento di Scienze della Terra "A. Desio," Università degli Studi di Milano, Via S. Botticelli 23, 20133 Milano, Italy.

[c] Norwegian University of Science and Technology (NTNU), Dep. of Geoscience and Petroleum, S. P. Andersens veg 15a, 7031 Trondheim, Norway.

[d] Department of Earth and Environmental Sciences, University of Milano-Bicocca, Piazza della Scienza 4, 20126 Milano, Italy.

[e] Sorbonne Université, Muséum National d'Histoire Naturelle, UMR CNRS 7590, IRD, Institut de Minéralogie, de Physique des Matériaux et de Cosmochimie, IMPMC, 4 Place Jussieu, 75005 Paris, France.

[f] Istituto di Geoscienze e Georisorse, Consiglio Nazionale delle Ricerche, Pisa, Italy.

* Corresponding author; mailto:francesco.ressico2@unibo.it; https://orcid.org/0000-0001-9020-7942 Piazza di Porta S. Donato, 1, 40126 Bologna BO

ABSTRACT

Subducted sections of dry oceanic mantle can undergo serpentinization through interaction with metamorphic fluids, recording a sequence of serpentinization events from the subseafloor to serpentine-out reactions. The geochemical patterns of these different stages of fluid-rock interaction trace the context and mechanisms of serpentinization processes. In this study, we used petrographic observations, micro-Raman spectroscopy, as well as bulk and *in situ* trace element analyses across a serpentinization front adjacent to a subduction-related tectonic contact in the Monte Maggiore massif, Alpine Corsica, France. Using a high-density sampling approach throughout the entire massif, we identified multiple and consistently distributed serpentine generations, reflecting successive hydration events in a chemically open system. Fluid-mobile elements (FME) exhibit a slight increase from lizardite- to antigorite-dominated generations and a more substantial rise with increasing serpentinization degrees towards the tectonic contact. When compared to other serpentinization fronts originated at different geodynamic settings – *e.g.*, Semail Ophiolite (Oman) as a subduction serpentinization front; Lanzo Massif (W. Alps) as a subducted oceanic serpentinization front–, the Monte Maggiore FME patterns indicate a subduction-related serpentinization front, rather than subducted oceanic serpentinites. Our results and the comparison with literature data suggest that decreasing *in situ* serpentine FME inventory concentrations across serpentinization fronts may be characteristic of subduction-zone serpentinization, whereas opposite trends may be diagnostic of subducted oceanic fronts. Our study also highlights the importance of tracing serpentinization as a spatially evolving process (across fronts), with least serpentinized rocks recording the latest stage(s) of serpentinization instead of relicts of incipient serpentinization.

1. INTRODUCTION

Serpentinization is the process of aqueous alteration of ultramafic rocks (Moody, 1976, Evans *et al.*, 2013, Schrenk *et al.*, 2013). The geochemical fingerprint of serpentinization within the first ten km of oceanic lithosphere together with the recycling of oceanic serpentinites during subduction have been the subject of multiple studies in the past decades (*e.g.*, Ranero *et al.*, 2003; Kelley *et al.*, 2005; Delacour *et al.*, 2008; Etiope and Sherwood Lollar, 2013; Scambelluri *et al.*, 2004; Hattori and Guillot, 2007; Kodolányi *et al.*, 2012; Pettke and Bretscher, 2022; Vesin *et al.*, 2024). While the possibility of serpentinization taking place at greater depths in subduction zones is known (*e.g.*, Bostock *et al.*, 2002; Hyndman *et al.*, 2003; Nozaka, 2005; Deschamps *et al.*, 2010; Vitale Brovarone *et al.*, 2017; Dandar *et al.*, 2019; Vitale Brovarone *et al.*, 2020; Boutier *et al.*, 2021), the mechanisms, reaction pathways, and geochemical framework of high-pressure serpentinization are poorly constrained. This process can affect both the supra-subduction forearc mantle (hereafter mantle wedge) and dry portions of subducting oceanic mantle rocks flushed by slab-derived metamorphic fluids. The subducted mantle lithosphere has the potential to record multiple stages of fluid-rock interaction from the subseafloor all the way down to the serpentine-out reaction in subduction zones (Evans, 2004; Debret *et al.*, 2013a; Padrón-Navarta *et al.*, 2013; Scambelluri *et al.*, 2014; Guillot *et al.*, 2015; Vitale Brovarone *et al.*, 2020). The geochemical composition of serpentinites partially reflects the chemistry of the aqueous fluid(s) responsible for the formation of serpentine minerals, which is in turn dependent upon fluid sources, geodynamic setting(s), and temperature (T) and pressure (P) conditions at which serpentinization takes place. Therefore, defining the characteristic geochemical patterns of high-T and high-P serpentinization relative to oceanic serpentinization, may provide insight to constrain their genetic context and relative implications in geochemical recycling at subduction zones. In this context, bulk and *in situ* trace element analysis is a powerful tool to study fluid-rock interactions, and has already been used to characterize serpentinization and its evolution in subduction zones (*e.g.*, Vils *et al.*, 2011; Debret *et al.*, 2013b; Lafay *et al.*, 2013; Peters *et al.*, 2017; Prigent *et al.*, 2018; Scambelluri *et al.*, 2019; Cannaò and Debret, 2024). These studies focused, in

74 particular, on the behaviour of fluid-mobile elements (FME: Li, B, As, Rb, Sr, Sb, Cs, Ba, Pb, and U
75 the latter under sufficiently oxidizing conditions) to track serpentinization events, fluid sources, and
76 the settings of serpentinization. Fluid mobile elements are indeed incorporated by serpentine minerals
77 during hydration and subsequently released during dehydration in subduction (*e.g.*, Scambelluri *et*
78 *al.*, 2015), providing information on the nature of slab fluids in subduction zones (*e.g.*, Vils *et al.*,
79 2011; Debret *et al.*, 2013b; Lafay *et al.*, 2013). In other cases, U versus alkalis and FME ratios
80 permitted to identify the environment of serpentinization, based on their chemical behaviour under
81 different redox conditions (Peters *et al.*, 2017).

82 Here, we present the case study of the partially serpentinized Monte Maggiore ultramafic
83 body, Alpine Corsica, France (Jackson and Ohnenstetter, 1981; Malavieille, 1983; Debret *et al.*, 2014;
84 Magott *et al.*, 2020). This body was initially part of a segment of the slow-spreading Piemonte-
85 Ligurian ocean and was then involved in Alpine subduction, reaching blueschist-facies conditions
86 (Malavieille, 1983; Rampone *et al.*, 2008; Rampone *et al.*, 2009; Piccardo and Guarnieri, 2010;
87 Debret *et al.*, 2014; Basch *et al.*, 2018). Regional-scale geological features indicate that the
88 serpentinization front of Monte Maggiore propagates from its basal tectonic contact, which
89 corresponds to a subduction-related Alpine fault (Malavieille 1983), into the ultramafic body. The
90 Monte Maggiore body may therefore represent an example of an oceanic mantle that did not interact
91 significantly with seawater during the oceanic stage and was subsequently subjected to multiple
92 serpentinization events during subduction. However, previous work suggests the presence of a
93 precursor oceanic serpentinization stage in the Monte Maggiore serpentinization front (Debret *et al.*,
94 2014). To unravel different hypotheses, or to confirm the latter, we adopted a high-density sampling
95 strategy (*i.e.*, 88 samples over a 4 km^2 area) aimed at mapping mineralogical and geochemical
96 variability across the Monte Maggiore serpentinization front. We investigated the distribution of
97 serpentine generations and their trace element concentrations, in particular FME, by means of laser
98 ablation inductively coupled plasma mass spectrometry (LA-ICP-MS). We discuss the most likely
99 serpentinization environments for the Monte Maggiore case study, and the characteristic trace

element signatures of high-pressure serpentinization relative to oceanic subducted serpentinites.

2. GEOLOGIC SETTING

The Monte Maggiore body is located in the northern part of the island of Corsica, France (Fig. 1). This body belongs to Alpine Corsica, a stack of variably metamorphosed units of oceanic and continental affinity overthrust onto the Corsica Hercynian basement during the Alpine orogenesis (Mattauer *et al.*, 1981; Durand-Delga, 1978, 1984; Jolivet *et al.*, 1998; Malavieille *et al.*, 1998; Molli and Malavieille, 2011; Vitale Brovarone *et al.*, 2013). The ocean-derived units of Alpine Corsica are equivalent to the Schistes Lustrés Complex of the Western Alps and represent segments of the slow-spreading Piemonte-Liguria oceanic basin including mafic and ultramafic rocks and their sedimentary cover sequences (Durand-Delga, 1978, 1984; Lagabrielle and Cannat, 1990; Lagabrielle *et al.*, 2015; Vitale Brovarone *et al.*, 2014). Slices and sedimentary horizons of continental affinity have been interpreted as representative of continental extensional allochthons characteristic of the rifting phase of the Piemonte-Liguria ocean (see Vitale Brovarone *et al.*, 2011, 2013; Beltrando *et al.*, 2014 and references therein). The Alpine metamorphic overprint varies from low-grade, to sub-greenschist to lawsonite eclogite-facies conditions (Vitale Brovarone *et al.*, 2013; and references therein for a review). Geochronological data indicate a Late Eocene age for the high-pressure metamorphic event in the Schistes Lustrés (Martin *et al.*, 2011; Vitale Brovarone and Herwartz, 2013; Rossetti *et al.*, 2015).

The Monte Maggiore body is a 4 km^2 massif consisting of a slightly to fully serpentinized mantle peridotite locally crosscut by mafic (mostly gabbroic) dykes of Jurassic age (Rampone *et al.*, 2008; Piccardo and Guarnieri, 2010; Basch *et al.*, 2018). It is interpreted as a portion of exhumed oceanic mantle impregnated by MORB-type magmas in an ocean-continent transition setting (OCT) (Jackson and Ohnenstetter, 1981; Piccardo and Guarnieri, 2010). Despite the remarkable preservation of mantle-derived assemblages (Rampone *et al.*, 2008; Piccardo and Guarnieri, 2010; Basch *et al.*, 2018), the Monte Maggiore body experienced blueschist-facies high-P metamorphism, as indicated

126 by the formation of nearly pure jadeite on igneous plagioclase (Jackson and Ohnenstetter, 1981;
127 Debret, 2013; Debret *et al.*, 2014).

128 The peridotite body is juxtaposed to the Centuri unit, which consists of a pre-Alpine crystalline
129 basement including ortho- and paragneiss, amphibolite, and minor marble layers, showing local
130 manifestations of blueschist-facies Alpine metamorphic overprint (Malavieille, 1983). The contact
131 between the Monte Maggiore ultramafic body and the underlaying Centuri unit is a 100-250 meters
132 thick, NNW-dipping shear zone originated during the Alpine subduction/orogeny (Malavieille,
133 1983). This shear zone is localized into the Centuri continental unit, with a strong strain gradient –
134 also visible from satellite images – towards the overlying Monte Maggiore body, and it is marked by
135 syntectonic high-P/low-T metamorphism (Malavieille, 1983). On the contrary, ductile deformation
136 in the Monte Maggiore body is only locally observed (Malavieille, 1983). A metasomatic horizon
137 composed of chlorite schists and/or mafic schists is present at the contact between the Centuri and
138 Monte Maggiore units (Jackson and Ohnenstetter, 1981).

139 Previous work on the Monte Maggiore ultramafic rocks documented two main zones characterized
140 by weakly serpentinized peridotites in the northern part of the massif, and serpentinites to the south,
141 respectively (Jackson and Ohnenstetter, 1981; Debret, 2013; Debret *et al.*, 2014; Magott *et al.*, 2020).
142 In between the two zones, ultramafic pseudotachylites are reported and interpreted as having formed
143 in response to seismic activity during Alpine subduction (Fabbri *et al.*, 2018; Magott *et al.*, 2020).
144 Two main serpentinization events were recognized (Debret, 2013; Debret *et al.*, 2014): the first was
145 interpreted to have formed during an oceanic stage of serpentinization, with the crystallization of
146 lizardite veins on primary mantle minerals; the second one is represented by the formation of
147 antigorite veins formed at the expense of lizardite and primary minerals during high-P metamorphism
148 conditions in the Alpine subduction zone. An alternative interpretation is presented in the present
149 study.

3. METHODS

3.1 Petrographic investigations and micro-Raman spectroscopic analysis

Petrographic and microstructural analyses were performed on a Zeiss correlative microscopy platform composed of an AxioZoom V16 macroscope, an AxioScope7 polarized microscope, and an EVO 15 scanning electron microscope (SEM) at the DeepCarbonLab, BiGeA Department, University of Bologna, Italy. The SEM was used to perform backscattered electron (BSE) imaging, in variable pressure mode, to highlight microstructural relationships among fine-grained serpentine generations. Raman analyses were performed on a WITec Alpha 300-R confocal micro-Raman spectrometer with a 532 nm laser source at the BiGeA Department, University of Bologna, Italy. The Raman spectra were acquired with a 100x objective and the following parameters: 600 g/mm grating; 25 mW on-sample laser power and acquisition time of 1 minute. The instrument is equipped with an Ar-Hg lamp integrated in the optical path, permitting the calibration of the Raman shift through the detection of Ar-Hg calibration lines during each analysis. The spectral regions from 200 to 1200 cm^{-1} and 3600 to 3750 cm^{-1} were investigated since they are characteristic for the distinction of serpentine polysomes. The acquired spectra of serpentine were compared with the data reported in Auzende *et al.* (2004), Groppo *et al.* (2006), Schwartz *et al.* (2013) and Compagnoni *et al.* (2021).

3.2 Bulk-rock major, minor/trace elements, and Fe_2O_3/Fe_{tot} ratios

Sixty-five samples were selected for determination of major element concentrations. Sample aliquots were obtained from the counterparts of rock chips used for thin section preparation. For each sample, the rock was pulverized with a Retsch PM400 by ball milling in agate jars. The concentration of major (SiO_2, TiO_2, Al_2O_3, Fe_2O_3, MnO, MgO, CaO, Na_2O, K_2O, P_2O_5) and some minor/trace (As, Ba, Co, Cr, Cu, Nb, Ni, Pb, Rb, S, Sr, V, Y, Zn, Zr) elements was determined using a wavelength dispersive X-ray fluorescence spectrometer (W-XRF) Panalytical Axios 4000, equipped with a Rh tube, at the XRF laboratory of BiGeA Department, Bologna. The analyses were performed on pressed powder pellets applying the Fundamental Parameters approach for matrix correction. The reproducibility of

major element measurements was generally better than 5 %, while it was better than 10 % on average for trace elements (see the Supplementary materials for specifics; e.g., S detection limits). The general accuracy was within the reproducibility range as determined by the analyses of Standard Reference Materials of comparable composition (HARZ-1, JP-1, PCC-1, UB-N, NIM-D, OU-7). The Loss On Ignition (LOI) was gravimetrically estimated after 12 h heating at 950°C in a muffle furnace (Heiri *et al.*, 2001). Ferric iron contents were measured by Ontario Geo Labs, Canada. Ferrous iron was determined by potentiometric analysis using potassium permanganate as oxidation agent. Ferric iron was calculated from the difference of the total iron measured by XRF and ferrous iron measured by potentiometric analysis.

3.3 In-situ trace elements

In situ trace element mineral concentrations were determined at the Geochemistry, Geochronology and Isotope Geology Laboratory of the Earth Science Department "A. Desio", University of Milano LA STATALE (Italy) by LA-ICP-MS. Analyses were conducted on 70 μm thick polished thin sections from 38 selected samples. These sections were prepared from the same sample chips as 30 μm thick sections that were used for preliminary petrographic observations. Petrographic features of the 70 μm set were crosschecked with the 30-μm, evidencing almost identical petrological aspects (*i.e.*, modal composition, serpentinization degree, serpentine generation assemblages). The instrument couples a 193nm ArF excimer laser ablation microprobe equipped with HelEx II volume sample chamber (Analyte Excite from Teledyne Photon Machines) with a single-collector quadrupole ICP-MS (iCAP RQ from Thermo Fisher Scientific). The carrier He flow rate was set to 0.54 l/min and to 0.32 l/min into the sample chamber and in the HelEx II cup, respectively. Laser spot size was chosen as large as possible for the analysed minerals (50 to 65 μm) in order to ensure the lowest limits of detection and single spot analyses were carefully positioned to avoid inclusions. However, due to sporadic micro inclusions of serpentine in metamorphic olivine, mixed analyses cannot be excluded for this mineral. The absence of contributions in the ablated material from solid/fluid inclusions was

202 further checked by inspecting the time-resolved spectra for chemical anomalies. The ablation system
203 was operated with a repetition rate of 10 Hz and an on-sample laser fluence of 2.0 J/cm^2 for olivine
204 and 3.0 J/cm^2 for serpentine. Each spot was analysed for a total of 120 s that included 40 s of
205 background analyses (comprising 10 s of laser warm-up), about 60 s of measuring mass peak intensity
206 followed by 20 s of wash-out time. The ARM-3 andesitic synthetic glass (Wu *et al.*, 2019) was used
207 as external standard, whereas ^{29}Si was selected as internal standard. Quality control was achieved
208 analysing the USGS BCR-2G reference glass (GEOReM database) as unknown in each analytical
209 run. Precision and accuracy are better than 10% for most elements (Supplementary materials). Data
210 reduction was carried out offline using the Glitter software package (Griffin *et al.*, 2008).
211
212 **4. RESULTS**
213 ***4.1 Field relations and petrography***
214 Figure 1 presents a revised geological map and the geometry of the Monte Maggiore serpentinization
215 front from earlier works (Jackson and Ohnenstetter, 1981; Debret, 2013; Basch *et al.*, 2018; Fabbri
216 *et al.*, 2018), and new data from two field surveys, along with 88 thin sections from the entire massif.
217 Based on the collected data, the Monte Maggiore serpentinization front is progressive, from full
218 serpentinization at its base, to almost absent in the uppermost part of the massif (Figs. 1 and 2).
219 Additionally, besides the first meters above the tectonic contact and a few localized deformation
220 zones, the Monte Maggiore serpentinites and partially serpentinized peridotite generally do not show
221 evidence of pervasive ductile deformation and shearing. Microscopic investigations indicate that, in
222 most cases, anisotropic structures observed in the hand specimen or in thin sections are determined
223 by sub-parallel sets of serpentine veins, statically crosscutting serpentinized peridotite structures.
224 These features suggest dominantly static serpentinization propagating from the basal tectonic contact
225 upwards.
226 Based on the data collected in this study, the massif can be subdivided into three main zones
227 that reflect their serpentinization degree, determined on visual estimation of each sample thin section

228 (Terry and Chilinger, 1955). These three zones correspond to well preserved peridotites (0 - 35 vol.
229 % serpentinization), partially serpentinized peridotites (35 - 75 vol. % serpentinization), and
230 serpentinites (75 - 100 vol. % serpentinization), respectively. Although the boundaries between these
231 zones are transitional in the field, Fig. 1 shows sharp boundaries for cartographic simplicity. About
232 90 % of these samples (number of samples, n = 78) were collected in the western part of the Monte
233 Maggiore body and allowed us to map lithological and mineralogical variations with a high spatial
234 resolution. Owing to limited exposure and weathering conditions, only 10 samples could be studied
235 from the eastern part of the body, leading to a lower spatial resolution relative to the western part.
236 Locations of the studied samples are reported in Figure 1 and in the Supplementary material, together
237 with their peridotite protolith rocks as inferred from petrographic analyses, and their main serpentine
238 mineral associations as defined by MicroRaman spectroscopy.
239
240 ***4.1.1 Preserved peridotites***
241 Preserved peridotites are mostly found in the northern and innermost part of the massif (Fig. 1) and
242 exhibit serpentinization degrees in the range of 0 - 35 vol. %. In the field, preserved peridotites are
243 often characterized by a strong reddish alteration on the weathered surface. These rocks appear mostly
244 undeformed, with local anisotropy being related to primary magmatic foliation (Jackson and
245 Ohnenstetter, 1981). Clinopyroxene (green in the hand specimen) and orthopyroxene (brown in the
246 hand sample) can be identified on weathered surfaces. Spinel often shows white rims of either
247 variably preserved plagioclase or chlorite. Based on the primary mineral assemblages, spinel-bearing
248 lherzolite, plagioclase-impregnated harzburgite, and dunite were identified in the field, in agreement
249 with previous work (see Rampone *et al.*, 2009; Basch *et al.*, 2018; Piccardo and Guarnieri, 2010).
250 Dunites and harzburgites are present as isolated pods, whereas lherzolites represent the most common
251 mantle rock type in the area (Fig. 1). Preserved peridotites are locally crosscut by gabbroic dykes
252 ranging from a few centimetres to several meters in thickness. The sharp boundary between ultramafic
253 hosts and mafic dykes is often marked by chlorite-antigorite-rich halos similar to serpentine veins

(black wall in Fig. 3a). In thin section, primary olivine (P-Ol), orthopyroxene (P-Opx), and clinopyroxene (P-Cpx) are mostly preserved. Spinel is generally, yet not systematically, surrounded by a fine-grained chlorite rim, and partially to fully replaced by magnetite. Fresh plagioclase is present but often replaced by epidote and chlorite. Preserved peridotites are most commonly crosscut by a pervasive network of 50 to 100 μm thick lizardite (Liz) veins, colourless to light green in plane polarized light (PPL), often associated with brucite, sulphides, and rare magnetite in the centre of the veins (Figs. 3e, 5a and 6). These veins correspond to V1 and V2 in Debret (2013). Lizardite veins form a pervasive network replacing mainly P-Ol and more rarely P-Opx. When altered, Liz exhibits a brown-yellowish colour in PPL. In some samples the Liz network is replaced and crosscut by 50-200 μm thick antigorite veins (Atg1), colourless in PPL, which in some cases also contains sulphides and Ni-alloys (Figs. 3e, 5a and 6). These veins are randomly to consistently oriented and show variable spacing. Both Liz and Atg1 generations are often crosscut by thin, colourless to greenish chrysotile veins. These are considered as late veins and will not be discussed further in this study. In a few samples of preserved peridotite where Liz network and Atg1 veins are rare, a successive generation of lizardite/antigorite mixtures (Liz/Atg) is found, forming sharp, 100 to 200 μm thick, veins (Figs. 3f, 5c, 5d and 6). This generation is replacive on P-Ol and less commonly on P-Opx. These veins are colourless in PPL, associated with fine- to medium-grained magnetite veins, and often contain fine-grained aggregates of colourless to brownish metamorphic olivine (M-Ol) (u). Liz/Atg veins generally show preferred orientation in thin section and can be also recognized at the outcrop scale (Fig. 3b). This generation is microstructurally older than colourless antigorite veins (Atg2), associated with rare Fe-Ni alloys (Fig. 5b). Antigorite2 replaces only primary mantle minerals and mainly P-Ol, forming blade-like aggregates departing from thin fractures (Figs. 3b, 6), or in association with Liz/Atg ± M-Ol veins at the rims of those veins (Figs. 3f, 5c, 5d). In some samples, the Liz network is almost absent and Atg2 is the most abundant serpentine generation in preserved peridotites, particularly in the inner part of the massif (Fig. 1). A last serpentine generation of

279 antigorite, Atg3, locally replaces Liz/Atg veins and the associated M-Ol, forming isolated colourless
280 blades (Figs. 3f, 5c, 5d, and 6).

281 ***4.1.2 Partially serpentinized peridotites***

282 Partially serpentinized peridotites comprise rocks showing serpentinization degrees in the range of
283 35 - 75 vol. %. These rocks structurally underly the preserved peridotite core and overlay the more
284 extensively serpentinized rocks towards the basal contact of the Monte Maggiore body. Gabbro dykes
285 occurring within this portion of the massif generally preserve relicts of the igneous mineralogy,
286 including plagioclase, and show variable degrees of alteration from high-T late magmatic to
287 metamorphic alteration. These rocks display a massive texture, with minor evidence of ductile
288 deformation. In the field, like for preserved peridotites, these rocks are characterized by reddish
289 weathering products on P-Ol. Pyroxenes are generally visible on the weathered surface, whereas
290 spinel and plagioclase domains are no longer recognizable. Despite the partial transformation of both
291 P-Ol and P-Opx, petrographic analysis allowed us to identify, in order of abundance, lherzolite,
292 harzburgite, and dunite protoliths (Fig. 1).

293 In thin section, primary plagioclase sites are still visible and replaced by chlorite and epidote-
294 rich assemblages (Figs. 4a, b). Primary spinel sites are partially replaced by chlorite and magnetite.
295 Primary olivine is commonly replaced by the associations Liz/Atg + Atg2 ± Atg3 ± M-Ol (Fig. 3f),
296 and Atg2 ± Atg3 ± M-Ol (Fig. 3g), while Liz is almost absent. These rocks show similar petrographic
297 and microstructural features observed in preserved peridotites, except for higher serpentinization
298 degrees and generally, more abundant M-Ol and thicker veins. Moreover, P-Opx is commonly
299 partially replaced by a single or double corona (brownish in thin section) of metamorphic Cpx
300 (hereafter M-Cpx; inner corona) and M-Ol (outer corona) and variable transformation to antigorite
301 (Atg2) along cracks and cleavage (Figs. 4 a, 4c, 4d). BSE images indicate that this M-Ol is richer in
302 Fe compared to P-Ol (see also Vitale Brovarone *et al.*, 2020 for similar textures), even though a
303 quantitative compositional assessment was not possible due to the small grain size and to the presence
304 of disseminated antigorite crystals (Fig. 4d).

Along the transition into the underlying serpentinites (>75 vol. % serpentinization), and particularly in the proximity of pseudotachylytes, serpentinized peridotites preserve pre-serpentinization cataclastic microstructures, including grain-size reduction of primary minerals and pervasive sets of fractures. Antigorite2 is the dominant serpentine generation replacing these structures, which are also visible in the field (Fig. 3c).

4.1.3 Serpentinites

Serpentinites show serpentinization degrees higher than 75 vol. %. This rock type constitutes the basal layer of the Monte Maggiore ultramafic body. It crops out mainly in the southern part of the massif and, to a lesser extent, in the northern part (Fig. 1). In the field, serpentinites appear to statically replace the precursor peridotite, with visible P-Cpx and P-Opx sites (Fig. 3d) and preserve the protolith structure with negligible ductile deformation (Figs. 2b, c). Most anisotropic structures are related to sub-parallel sets of serpentine veins cutting across statically serpentinized matrices. Foliated serpentinites are limited to isolated cm-sized domains located in the southern-central part of the massif, within the bottom meters of serpentinites above the basal tectonic contact (Figs. 2a, c). The foliation is generally consistent with the orientation of the basal tectonic contact, dipping towards N-NW at an angle of 20 - 45° (Fig.1).

In thin section spinel is replaced by magnetite and often surrounded by a chlorite corona. Plagioclase is completely altered into epidote and chlorite. Based on microstructural relationships, Liz/Atg is the oldest generation, appearing colourless in PPL and forming mesh-like textures (Fig. 3h). It is typically associated with fine- to medium-grained magnetite, the latter occurring as disseminated crystals in the veins or forming aggregates in their central part (Figs. 3h, 5e, 5f). This generation of serpentine likely formed at the expense of P-Ol and P-Opx, although the intense serpentinization degree does not allow for more accurate evaluations. In some cases, P-Opx sites are still visible due to the presence of magnetite trails marking former P-Opx cleavages (Fig. 5f) (see also Plümper *et al.*, 2017; Boutier *et al.*, 2021). In several samples, fully serpentinized P-Opx sites are

rimmed by a corona of fine-grained M-Cpx (Figs. 4e, f). Lizardite-antigorite mixtures are petrographically equivalent to Liz/Atg described above.

This generation is partially to completely substituted by a successive serpentine generation, which preserves the previous texture of Liz/Atg. It occurs as disseminated static flakes, patches and veins crosscutting previous structures, or partially replacing P-Cpx relicts (Fig. 2h). This generation is constituted by antigorite and referred to as Atg3 by analogy with Atg3 observed in partially serpentinized peridotites. It is colourless in PPL and commonly associated with magnetite, but in lesser amounts compared to the previous generation. In deformed serpentinites a final generation of colourless antigorite (Atg4) occurs as precipitate in deformed thick fractures, lacking any association with opaque minerals compared to the surrounding serpentine generations (Figs. 3h, 5f, 6). Atg3 and Atg4 are generally more abundant in deformed serpentinites found in the proximity of the tectonic contact or as isolated deformed domains inside the Monte Maggiore massif.

To sum up, the types and distribution of serpentine generations in the Monte Maggiore ultramafic body can be described by four main mineral associations (indicated with roman numbers below), which are not necessarily related to a chronological order, but rather to a spatial distribution in the massif (refer to Fig. 1 and synoptic table in Fig. 3 for their relative distribution within the massif):

I) The Liz1 ± Atg1 association, which occurs only in the preserved peridotites (0 - 35 vol. % serpentinization) in the inner part of the massif, the area farthest from the tectonic contact.

II) The Liz/Atg + Atg2 ± Atg3 ± M-Ol association, which occurs in both preserved and partially serpentinized peridotites (0 - 75 vol. % serpentinization).

III) The Atg2 ± Atg3 ± M-Ol association, which can occur in both preserved and partially serpentinized peridotites, but more specifically in the deformed areas at the interface with serpentinites.

356 *IV)* The Liz/Atg ± Atg3 ± Atg4 association, which only occurs in serpentinites (>75 vol. %
357 serpentinization), in proximity of the tectonic contact.
358
359 ***4.1.4 Centuri gneiss***
360 Hereafter, we describe some key features of the mylonitic zone marking the uppermost part of the
361 Centuri gneiss, in contact with the overlying Monte Maggiore massif. The mylonite affects the
362 Centuri gneiss, which shows a progressive chemical variation towards the contact with the Monte
363 Maggiore massif, from pelitic to mafic compositions of plausible metasomatic origin. The top 10
364 meters of the Centuri mylonite are dominated by fine-grained, greenschist-facies assemblages
365 including abundant epidote, green amphibole, and albite, with relict blue amphibole. Local lithons
366 inside the mylonite preserve blueschist-facies assemblages including blue-amphibole, epidote, and
367 Na-clinopyroxene pods, and marking a previous mylonitic stage that was subsequently folded (Figs.
368 2d, g).
369
370 ***4.2 Whole rock major elements composition***
371 Whole-rock major element compositions are presented in the Supplementary material and in Figure
372 7, together with previous data from the literature (Romairone, 1996; Rampone and Piccardo, 2008;
373 Piccardo and Guarnieri 2010). The olivine-clinopyroxene-orthopyroxene ternary diagram of Figure
374 7a shows the comparison between protolith determination and serpentinization degree on an optical
375 microscopy basis, and normative mineralogy calculation (CIPW) based on whole-rock chemical
376 analyses (following the method by Kelemen *et al.*, 1992, considering Fe_{tot} as FeO). The results from
377 Figure 7a clearly show that a progressive transition from Opx-poor to Opx-rich normalized
378 compositions accompanies the progressive increase of serpentinization degree from the core of the
379 Monte Maggiore body towards its basal contact. However, potential artifacts related to the selected
380 CIPW normalization procedure for variably serpentinized peridotites can be identified. For example,
381 several samples show inconsistent optic and CIPW classifications. Moreover, the abundance of rocks

382 plotting between the dunite-wehrlite transition is not supported by previous mantle petrology studies
383 (Romairone, 1996; Rampone and Piccardo, 2008; Piccardo and Guarnieri 2010). A progressive
384 decrease of MgO/SiO_2 ratios with increasing serpentinization is also shown by Figure 7b, with Monte
385 Maggiore serpentinites plotting below the terrestrial array for mantle rocks. The Al_2O_3/SiO_2 ratio is
386 generally lower in harzburgites and dunites relative to lherzolites. In Figure 7c, SiO_2 and MgO values
387 are presented recalculated on an anhydrous basis. It can be observed that, for preserved peridotites (0
388 - 35 vol. % serpentinization), a clear correlation between MgO and SiO_2 exists and reflects the
389 chemical composition of the protolith. In contrast, more serpentinized rocks (> 35 vol. %
390 serpentinization) show enrichment in SiO_2 relative to preserved peridotites and no clear trend relative
391 to MgO (Fig. 7c). Figure 7d shows, through an Fe_2O_3/Fe_{tot} versus MgO/(MgO+FeO) diagram, the
392 presence of a positive correlation and two distinct populations corresponding to preserved/partially
393 serpentinized peridotites and serpentinites, with the latter exhibiting higher values for both ratios.
394
395 ***4.3 In-situ trace element compositions***
396 According to major element results (see section 4.2) data can be subdivided in two distinct groups.
397 The first group includes preserved peridotites and partially serpentinized peridotites, which show
398 comparable trace element patterns (Figs. 8, 10); the second group includes only serpentinites (Figs.
399 9, 10). Since the aim of this study is to highlight differences in the concentrations of fluid-mobile to
400 less fluid-mobile elements (FME) in different serpentine generations, particular emphasis will be
401 given to serpentine generations belonging to a consistent microstructural domain, in particular
402 serpentine generations overgrowing (rock's matrix) or cutting (veins) P-Ol. In section 4.3.2, we will
403 give a general description of FME trends relative to Primitive Mantle (PM, McDonough and Sun,
404 1989). Absolute FME (Li, B, As, Rb, Sr, Sb, Cs, Ba, Pb, U) concentrations are presented to assess
405 variations across the Monte Maggiore serpentinization front (Fig. 10). Antimony and As
406 concentrations are not shown in Figure 10 because too many analyses were below the detection
407 limits (bdl). The full dataset is presented in the Supplementary material.

4.3.1 Rare Earth Element patterns

4.3.1.1 Preserved peridotites and partially serpentinized peridotites

For the majority of the obtained results, with the exception of sample COR22-13 which will be discussed separately in this section, Rare Earth Element (REE) patterns of serpentine minerals match the primary mineral in the considered microstructural domain, generally displaying a positive slope within light to medium rare elements (LREE-MREE) (La_N/Gd_N = 0.002 - 0.535), and a slightly positive to flat and negative slope from medium to heavy REE (MREE-HREE; Gd_N/Lu_N = 0.025 - 2.20) (Figs. 8a-f). Several data-points show intermediate compositions between precursor P-Ol and P-Opx. This feature seems to depend on the relative contribution of P-Ol or P-Opx, as described by previous authors (*e.g.*, Andreani *et al.*, 2009; Deschamps *et al.*, 2010; Lafay *et al.*, 2013; Debret et al, 2013b). The dependence of the REE pattern on microstructural features was generally observed for Liz, Atg1, Atg2, and Atg3. Nevertheless, for some analyses, in particular for the majority of Liz/Atg and M-Ol spot analyses, the REE patterns of crystals formed at the expense of P-Ol are rather similar to P-Opx within the LREE-MREE interval and to an intermediate composition between P-Ol and P-Opx within HREE interval. For Atg2, a set of analyses from a single sample (COR22-13) characterized by vein networks that are thicker and more pervasive than average show higher LREE concentrations, resulting in an almost positive to flat REE pattern (La_N/Lu_N = 0.273 - 1.44).

4.3.1.2 Serpentinites

The REE of Liz/Atg, Atg3, and Atg4 show three main patterns (Figs. 9a-c): i) REE depletion, resembling the P-Ol compositions; ii) LREE depletion similar to P-Opx in the LREE segment and a mixture between P-Ol and P-Opx in the MREE-HREE segment; and iii) flat patterns similar to P-Cpx compositions in the LREE segment and an intermediate composition between P-Ox and P-Ol in the MREE-HREE segment. Rare earth element patterns of Liz/Atg, Atg3, and Atg4 in serpentinites generally show higher concentrations relative to the same generations in preserved to partially serpentinized peridotites.

4.3.2 Fluid-mobile elements in the serpentine generations

4.3.2.1 Preserved peridotites and partially serpentinized peridotites

Compared to primitive mantle (PM) (Figs. 8g-n), all studied serpentine generations in preserved and partially serpentinized peridotites are considerably enriched in B (up to 120 × PM values). The other FMEs are commonly below PM values, with a few exceptions for specific serpentine generations. Antimony, As, and Cs, are moderately enriched relative to PM in a few analyses of Liz, Liz/Atg, Atg1, and Atg2 (Sb up to 20 × PM; As up to 35 × PM; Cs up to 3 × PM; Li up to 2 × PM). A positive Pb anomaly is commonly observed in PM-normalized spider diagrams, especially in Liz (Pb_N/Pr_N = 55; Pb_N/Pr_N = 30), Liz/Atg (Pb_N/Pr_N = 18; Pb_N/Pr_N = 17) and Atg3 (Pb_N/Pr_N = 10; Pb_N/Pr_N = 7) (Figs. 8g, h, n). Some analyses of Atg1 and Atg3 are depleted in Pb, relative to PM, and are commonly bdl. Rubidium, Ba, Sr, and U are always depleted relative to PM. Like serpentine minerals, also M-Ol is enriched in FMEs such as B, Li relative to PM (B up to 30 × PM; Li up to 7 × PM), and in some cases in less immobile elements like Lu (Lu almost up to 2 × PM). Metamorphic olivine may contain tiny inclusions of serpentine, which may affect the quality of La-ICP-MS analyses and the concentrations of trace elements, in particular B and Sr.

Liz displays low concentrations in B (1.30 – 11.6 µg/g, median = 3.84 µg/g), Sr (0.005 - 0.478 µg/g, median = 0.154 µg/g), Cs (0.047 - 0.049 µg/g, median = 0.048 µg/g) and Ba (0.009 - 0.320 µg/g, median = 0.027 µg/g), which is most of the time bdl (Fig. 10). Liz displays instead high concentrations in Rb (0.075 - 0.670 µg/g, median = 0.156 µg/g), and moderate concentrations in Pb (0.021 - 0.138 µg/g, median = 0.052 µg/g) and U (0.001 - 0.002 µg/g, median = 0.001 µg/g) (Fig. 10).

Liz/Atg is enriched in Sr (0.107 - 5.78, median = 1.37 µg/g), and Pb (0.020 - 0.896 µg/g, median = 0.065 µg/g), which is particularly enriched in preserved peridotites (0.142 - 0.896 µg/g, median = 0.574 µg/g) compared to partially serpentinized peridotites (0.020 - 0.194 µg/g, median = 0.049 µg/g) (Fig. 10). The rest of FME display substantially intermediate concentrations (Li: 0.270 - 2.09 µg/g, median = 0.690 µg/g; B: 1.25 - 62.2 µg/g, median = 6.46 µg/g; Rb: 0.041 - 0.160 µg/g,

459 median = 0.072 µg/g; Cs: 0.014 - 0.035 µg/g, median = 0.030 µg/g; Ba: 0.007 - 1.74 µg/g, median =
460 0.072 µg/g; U: max 0.001 µg/g, median is bdl) (Fig. 10).

461 Antigorite1 and Atg2 share similar concentrations in Li (0.204 - 1.99 µg/g, median = 0.459
462 µg/g; 0.260 - 1.61 µg/g, median = 0.592 µg/g respectively), B (1.46 - 15.0 µg/g, median = 6.69; 0.900
463 - 35.7 µg/g, median = 7.35 µg/g respectively), Sr (0.007 - 1.05 µg/g, median = 0.200 µg/g µg/g; 0.021
464 - 6.59 µg/g, median = 0.221 µg/g respectively) and Ba (0.013 - 0.259 µg/g, median = 0.044 µg/g;
465 0.004 - 1.24 µg/g, median = 0.05 µg/g respectively) (Fig. 10). Antigorite2 is more enriched in Rb
466 (0.051 - 0.184 µg/g, median = 0.118 µg/g), Cs (0.009 - 0.058 µg/g, median = 0.031 µg/g), Pb (0.028
467 - 0.187 µg/g, median = 0.048 µg/g), and U (maximum = 0.013 µg/g, median = 0.001), compared to
468 Atg1, which typically shows concentrations below detection limit for these elements except for a few
469 point analyses (Cs: 0.009 - 0.058 µg/g, median = 0.031 µg/g, bdl = 68% of analyses; Rb 0.051 - 0.184
470 µg/g, median = 0.118, bdl = 89% of analyses; Pb 0.028 - 0.187 µg/g, median = 0.048 µg/g, bdl = 86%
471 of analyses; U maximum = 0.002 µg/g, median = 0.001 µg/g, bdl = 86% of analyses) (Fig. 10).

472 Antigorite1 and Atg2 show different patterns across the serpentinization front. Antigorite1
473 displays a substantial, systematic increase in B, Sr, and Ba from preserved peridotites (B: 1.46 - 3.20
474 µg/g, median = 2.04 µg/g; Sr: 0.008 - 0.297 µg/g, median = 0.049 µg/g; Ba: 0.013 - 0.029 µg/g,
475 median = 0.021 µg/g) to partially serpentinized peridotites (B: 4.66 - 15.0 µg/g, median = 8.11 µg/g;
476 Sr: 0.068 - 1.05 µg/g, median = 0.357 µg/g; Ba: 0.014 - 0.259 µg/g, median = 0.116 µg/g) (Fig. 10).
477 Conversely, Atg2 shows a slight decrease in B, Sr, and Ba concentrations from preserved peridotites
478 (B : 2.73 - 35.7 µg/g, median = 11.2 µg/g; Sr: 0.073 - 6.59 µg/g, median = 0.848 µg/g; Ba: 0.005 -
479 0.392, median = 0.111 µg/g) to partially serpentinized peridotites (B: 0.900 - 30.5 µg/g, median =
480 4.87 µg/g; Sr: 0.021 - 1.39 µg/g, median = 0.212 µg/g; Ba: 0.004 - 1.24 µg/g, median = 0.034 µg/g
481 respectively), and an increase in U from preserved peridotites (always bdl) to partially serpentinized
482 peridotites (min = 0.001– 0.013 µg/g, median = 0.002 µg/g) (Fig. 10).

483 M-Ol is particularly enriched in Li (1.83 - 10.6, median = 4.01 µg/g), Sr (0.120 - 3.99 µg/g,
484 median = 1.12 µg/g), and Ba (0.031 - 4.70 µg/g, median = 0.840 µg/g), while it displays intermediate

concentrations in B (2.55 - 9.89 µg/g, median = 5.80 µg/g). Rubidium, Cs, Pb and U are, except for few analyses, mostly below the detection limit (Fig. 10).

Antigorite3 displays intermediate to high concentrations in Li (0.319 - 1.14 µg/g, median = 0.960 µg/g), B (1.53 - 26.5 µg/g, median = 11.5 µg/g), Sr (0.074 - 6.06 µg/g, median = 0.395 µg/g), and Ba (0.013 - 0.624 µg/g, median = 0.073 µg/g) (Fig. 10), whereas its concentrations are almost always below detection limit for Cs, Rb, Pb and U (Fig. 10).

4.3.2.2 Serpentinites

Relative to PM, Liz/Atg, Atg3, and Atg4 in serpentinites are on average enriched within the same factors in B (up to 300 × PM), Sb, and As (both often exceeding 30 × PM). Atg4 is particularly enriched in Cs (up to 80 × PM) and Rb (up to 2 × PM) compared to PM. Uranium contents are, on average, below PM values, except for a few analyses of Liz/Atg, Atg3, and Atg4 where high values from sample COR21-50 stand out from the rest of the analyses (up to 40 × PM) (Figs. 9d-f). A positive Pb anomaly is found in Liz/Atg (Pb_N/Pr_N = 4.5; Pb_N/Pr_N = 4.0) and Atg3 (Pb_N/Pr_N = 3.3; Pb/Pr_N = 3.6), on average below PM values, whereas in Atg4 Pb is always below detection limit except for one analysis (Fig. 9f). In PM-normalized spider diagrams (Figs. 9d, e), Hf and Zr anomalies are present in sample COR21-22c in Liz/Atg (Zr_N/Sm_N = 5.4; Zr_N/Eu_N = 5.4), and for one analysis of Atg3 from the same sample.

Liz/Atg, compared to the respective generation in partially serpentinized peridotites, shows higher concentrations in B (1.36 – 58.7 µg/g, median = 15.6 µg/g), As (0.310 – 1.12 µg/g, median = 0.350 µg/g), Sb (0.051 – 0.097 µg/g, median = 0.060 µg/g), Rb (0.055 – 0.268 µg/g, median = 0.101 µg/g), and U (maximum = 0.133 µg/g, median = 0.001 µg/g), whereas it shows a strong depletion in Li (0.217 - 0.790 µg/g, median = 0.313 µg/g) and to a lesser extent in Pb (0.019 - 0.218 µg/g, median = 0.047- 3.34 µg/g, median = 0.085 µg/g), and it shows comparable values compared to Liz/Atg in less serpentinized samples relative to other generations. Strontium (0.034 - 3.79 µg/g, median = 0.862

510 μg/g) and Ba (0.004 - 3.34 μg/g, median = 0.085 μg/g) show comparable values compared to Liz/Atg
511 in less serpentinized samples.
512 Antigorite3 concentrations substantially overlap with those of Liz/Atg for the majority of
513 FME such as B (1.60 - 88.2 μg/g, median = 16.3 μg/g), Sr (0.025 - 8.23 μg/g, median = 1.22 μg/g),
514 Sb (0.042 - 0.176 μg/g, median = 0.056 μg/g), Cs (0.016 - 0.170 μg/g, median = 0.039 μg/g), Ba
515 (0.004 - 13.2 μg/g, median = 0.118 μg/g), Pb (0.013 - 0.192 μg/g, median = 0.049 μg/g), and U
516 (maximum = 0.841 μg/g, median = 0.001 μg/g), with the exception of Li (0.211 - 0.880 μg/g, median
517 = 0.550 μg/g), As (0.290 - 1.67 μg/g, median = 0.594 μg/g), and Rb (0.045 - 0.379 μg/g, median =
518 0.144 μg/g) which are enriched relative to Liz/Atg (Fig. 10). When comparing Atg3 in serpentinites
519 to Atg3 in partially serpentinized peridotites, it emerges that almost all FME (B, As, Sr, Sb, Rb, Cs,
520 Ba, Pb, U), except Li, are present in higher concentrations in more serpentinized rocks (Fig. 10).
521 Antigorite4 shows high values in B (2.31 - 137 μg/g, median = 21.1 μg/g), Rb (0.035 - 1.20
522 μg/g, median = 0.192 μg/g), and Cs (0.099 - 1.64 μg/g, median = 0.206 μg/g), whereas it shows
523 intermediate concentrations in Li (0.330 -1.06 μg/g, median = 0.533 μg/g), As (0.266 - 0.900 μg/g,
524 median = 0.700 μg/g), Sr (0.087 - 15.6 μg/g, median = 0.880 μg/g), Sb (0.043 - 0.085 μg/g, median
525 = 0.058 μg/g), Ba (0.025 - 27.5 μg/g, median = 0.129 μg/g), and U (maximum = 0.193 μg/g, median
526 = 0.001 μg/g) (Fig. 10). Lead is almost always bdl.
527 From a global perspective it emerges that the percentage of analyses on FME below detection limit
528 (**Σ**FME /analyses$_{tot}$) in serpentine generations increase with the serpentinization degree, moving from
529 56% in S, to 66% in partially serpentinized peridotites and 70% in preserved peridotites.
530
531 **5. DISCUSSION**
532 ***5.1 Chronology and mechanisms of serpentinization events***
533 The Monte Maggiore massif is characterized by a serpentinization front propagating from the tectonic
534 contact with the underlying Centuri gneisses and decreases towards the core of the peridotite body

535 (Jackson and Ohnenstetter, 1981; Malavieille 1983; Rampone *et al.*, 2008; Rampone *et al.*, 2009
536 Piccardo and Guarnieri, 2010; Debret, 2013; Debret *et al.*, 2014; Basch *et al.*, 2018).

537 The massif was interpreted by previous authors as a fragment of oceanic mantle exhumed
538 during the formation of the Piemont-Ligurian basin in the Jurassic (*e.g.*, Jackson and Ohnenstetter,
539 1981; Piccardo and Guarnieri, 2010). Serpentinites were interpreted to have formed through
540 subseafloor peridotite hydration and subsequently subducted to blueschist-facies metamorphic
541 conditions (Debret, 2013; Debret *et al.*, 2014). The basal contact of the massif is, however, an Alpine
542 tectonic contact (Malavieille 1983). Mylonitic fabrics along the contact are predominantly developed
543 in the Centuri gneiss, whereas in the Monte Maggiore body, ductile deformation is very limited and
544 restricted to the first 10 - 20 meters above the contact (Fig. 2). Debret (2013) described a wider
545 foliated zone that was interpreted as a pre-Alpine serpentinization front characteristic of slow-
546 spreading oceans like the Piemont-Ligurian basin. However, this deformed zone could not be
547 identified during our field and petrographic survey. High strain zones are localized inside the
548 underlying Centuri gneiss or its metasomatic equivalents adjacent to the contact. Serpentinization in
549 the Monte Maggiore body appears structurally related to the tectonic juxtaposition with the Centuri
550 gneiss along a progressive and rather static serpentinization front. Besides orogenic belts,
551 serpentinites and continental basement slices may also characterize the distal portion of hyper-
552 extended margins, as documented in present-day settings and their metamorphosed equivalents in
553 mountain belts, including Alpine Corsica (Vitale Brovarone *et al.*, 2011; Beltrando *et al.*, 2014), and
554 be subsequently reactivated during subduction. However, the absence of intense deformation within
555 the serpentinized base of the Monte Maggiore body (Fig. 2) rules out that preexisting subducted
556 serpentinites were reactivated along an Alpine shear zone, since serpentinites would deform easily
557 during Alpine shearing along such a major tectonic contact. In the eclogite-facies units of Alpine
558 Corsica, serpentinites in contact with pre-Alpine continental extensional allochthons locally show no
559 marked deformation, on both sides of the contact (Vitale Brovarone *et al.*, 2011; Beltrando *et al.*,
560 2014). The large Alpine mylonite affecting the Centuri gneiss and the lack of significant ductile

561 deformation in the overlying serpentinite suggest that the Monte Maggiore ultramafic body was
562 relatively dry during the development of the basal tectonic contact and that it was hydrated in the
563 Alpine subduction zone.

564 The detailed petrographic characterization reported in this study, based on a high-spatial
565 resolution mapping of serpentine generations across the Monte Maggiore serpentinization front and
566 coupled with the distribution of multiple serpentine generations and their characteristic trace element
567 patterns, can be used to better unravel serpentinization processes of the Monte Maggiore body. The
568 collected data, together with literature one, allow us to describe the Monte Maggiore serpentinization
569 front as continuous and characterized by a progressive decrease in serpentinization degree from the
570 bottom to the top of the massif. Beside the first meters above the contact, the rather static deformation
571 inside the Monte Maggiore massif rules out the possibility of an internal tectonic juxtaposition of
572 multiple ultramafic slices during the Alpine tectonic evolution.

573 Within this serpentinization front, different serpentine generations and associations of
574 generations are observed in a consistent way throughout the massif. The formation of serpentine
575 polysomes and their associations has long been used to infer T conditions of serpentinization (*e.g.*,
576 Evans et al 2004; Schwartz *et al.*, 2013; Lafay *et al.*, 2013; Debret *et al.*, 2013a). Lizardite and
577 chrysotile are the main phases stable in low-T settings such as hydrothermal or low-grade
578 metamorphism (T < 300 °C), whereas antigorite is the high temperature (HT) polysome (T >300 °C;
579 Evans, 2004). In subduction systems, prograde replacement of lizardite to antigorite with increasing
580 T is observed between 320 and 390 °C and attested to by lizardite-antigorite mixtures (Schwartz *et*
581 *al.*, 2013). Finally, dominant antigorite is found from about 400 °C to its full breakdown to olivine +
582 talc +H_2O (P <2.0 GPa) or olivine + enstatite + H_2O (P >2.0 GPa) (Ulmer and Trommsdorff, 1995;
583 Padron-Navarta *et al.*, 2013).

584 The Monte Maggiore body is characterized by the presence of six main serpentine generations,
585 distinguished on the basis of characteristic polysomes, microstructural position, and crosscutting
586 relationships. They are Liz veins, Liz/Atg mixtures, Atg1 veins replacing previous lizardite, Atg2

587 replacing primary mantle minerals, Atg3 replacing previous Liz/Atg and M-Ol generations, and Atg4
588 veins precipitating in fractures. The different serpentine generations and M-Ol were also recognized
589 in four main recurrent associations corresponding to specific structural positions in the massif, and
590 hence across the serpentinization front: (I) Liz ± Atg1; (II) Liz/Atg + Atg2 ± M-Ol ± Atg3; (III) Atg2
591 ± Atg3 ± M-Ol; (IV) Liz/Atg ± Atg3 + Atg4 (see Fig. 1 for the distribution in the massif). These
592 associations do not necessarily have chronological meaning, but rather suggest multiple events of
593 serpentinization selectively affecting specific domains of the massif. As a whole, the spatial
594 distribution of these associations indicates a general increase in the antigorite proportion relative to
595 other serpentine generations towards the basal tectonic contact. These four associations of serpentine
596 generations result from protracted fluid-rock reactions and P-T evolution of the Monte Maggiore
597 ultramafic body, which may be interpreted in multiple ways, as summarized in Figure 11: prograde
598 replacement (Fig. 11a), changes in chemical conditions (SiO_2 addition) (Fig. 11b), evolving thermal
599 state of the subduction setting (Fig. 11c). The observed chronology of serpentine generations and the
600 distribution of associations of serpentine generations could be explained by a prograde sequence of
601 hydration events during Alpine subduction (Fig. 11a), as classically done in Alpine serpentinites
602 (Schwartz *et al.*, 2013; Debret *et al.*, 2013a). The stability of serpentine polysomes, however, is not
603 only T-dependent, but it can also be affected, for instance, by the chemistry of the fluid-rock system
604 in the case of lizardite stability relative to that of antigorite, and vice-versa (Rouméjon *et al.*, 2019).
605 Accordingly, the chronology and association of lizardite and antigorite generations in the Monte
606 Maggiore massif may also be explained by changing chemical conditions, where high silica activity
607 (a_{SiO2}) promotes the formation of antigorite over lizardite at low-T conditions (Rouméjon *et al.*, 2019)
608 (Fig. 11b). In the Monte Maggiore serpentinized peridotites, primary Opx is commonly transformed
609 into serpentine early in the serpentinization history, together with or even before olivine based on
610 microstructures from partially serpentinized peridotites. Previous works indicate that this
611 serpentinization pattern requires T conditions >400 °C (Martin and Fyfe, 1970; Oelkers and Schott,
612 2001; Allen and Seyfried, 2003). The presence of M-Ol coronas replacing P-Opx or rimming P-Ol

and showing higher Fe content relative to P-Ol, have been documented in partially serpentinized peridotites interpreted to have formed in the Apline subduction zone in Corsica (Vitale Brovarone *et al.*, 2020).

Local high SiO_2 contents promoted by Opx consumption may have favoured antigorite formation over lizardite or may have shifted the lizardite-antigorite transition to lower T. High SiO_2 contents affecting the stability of different serpentine polysomes may also result from infiltration of external fluids. By considering a compilation of bulk chemical data of oceanic serpentinites and thermodynamic modelling, Malvoisin (2015) concluded that serpentinization is an open-system process, with SiO_2 addition from associated mafic rocks and MgO loss by brucite dissolution with increasing fluid/rock ratio (F/R) relative to the starting peridotite composition. In a similar way, in Monte Maggiore, bulk rock MgO/SiO_2 ratios are observed to decrease with increasing serpentinization degree (Fig. 7b), suggesting either MgO loss or SiO_2 gain, or both. Bulk chemical data recalculated on an anhydrous basis indicate that SiO_2 increases with serpentinization degree, whereas MgO does not shows any trends compared to serpentinization degree (Fig. 7c). This feature may be explained by the infiltration of aqueous fluids enriched in SiO_2 during serpentinization. For instance, fluids produced from partial dehydration of minerals in the underlying Centuri (epidote, mica, talc, chlorite, blue amphibole and Na-Al-pyroxene) (see section 4.1.4), or other externally derived aqueous fluids equilibrated with the Centuri gneiss may have transported SiO_2 into the Monte Maggiore ultramafic rocks. This SiO_2 gain can be also observed in Figure 7a, with CIPW-normalized compositions of serpentinized rocks moving towards the Opx corner of the olivine-orthopyroxene-clinopyroxene ternary diagram. This increase in SiO_2 may have favoured increasing a_{SiO2} and the formation of antigorite over lizardite during prograde, low-T conditions. Alternatively, lizardite *vs.* antigorite formation may also be modulated by Al_2O_3 concentrations: experimental studies demonstrate that high Al_2O_3 concentrations extend the lizardite stability field to higher T where antigorite is generally expected to form (Caruso and Chernosky, 1979; Nakatani and Nakamura, 2016). In the Monte Maggiore rocks, mobilization of Al during serpentinization is primarily

639 controlled by spinel conversion to chlorite. Several studied samples show spinel replacement by
640 chlorite. Lizardite-bearing generations, however, are found in samples containing both fresh and
641 retrogressed spinel, ruling out the possibility of a chemically controlled HT lizardite formation.
642 In summary, the data collected across the Monte Maggiore serpentinization front suggest that
643 the formation of antigorite-rich serpentinites in the fully serpentinized portion of the massif started at
644 lower T conditions (full olivine serpentinization; minor to full Opx serpentinization) and that it was
645 possibly favoured by the infiltration of SiO_2-rich fluids and evolved at higher T in both fully and
646 partially serpentinized domains. The latter hypothesis is suggested by the transformation of P-Opx in
647 the olivine stability field, as observed in some partially serpentinized samples containing rather fresh
648 P-Ol and M-Ol forming at the expense of P-Opx (Figs. 4c, d). This indicates that a high T
649 serpentinization event took place in a relatively narrow range of T conditions from about 400 °C (P-
650 Opx destabilization in the olivine stability field in partially serpentinized peridotites; Martin and Fyfe,
651 1970; Oelkers and Schott, 2001; Allen and Seyfried, 2003) to about 450 °C (metamorphic peak of
652 Monte Maggiore), and under varying chemical conditions. Larger uncertainties remain for the timing
653 and conditions of Liz and Atg1 formation, which may span from oceanic to low-T conditions. The
654 lack of ductile deformation in the Monte Maggiore body, and the marked ductile deformation in the
655 underlying Centuri gneiss suggest that, even if serpentinization events predating the juxtaposition of
656 Monte Maggiore onto Centuri existed, such as oceanic or low-T serpentinization events, the bulk
657 serpentinization was recorded in response to fluid infiltration along their tectonic contact.
658 An alternative model to explain varying serpentine assemblages within a subduction zone
659 environment follows the recent definition of dynamic thermal states of subduction zones by Holt and
660 Condit (2021). The authors showed that the thermal state of subducting slabs changes from
661 subduction infancy to maturity, from warmer to colder thermal regimes (Fig. 11c). This model, which
662 has never been applied to varying serpentine polysomes so far, may explain at stationary depth
663 conditions – for example, at the base of the mantle wedge in the forearc regions – the retrograde
664 transition from antigorite to lizardite stability fields with subduction maturity. However, such

665 retrograde evolution is not observed in Monte Maggiore, ruling out the hypothesis of evolving thermal
666 states.
667 Based on the above discussion, the sequence of the serpentine generations points out that the Monte
668 Maggiore ultramafic body recorded several steps of hydration in response to progressive subduction
669 and increasing T (Fig. 11a) and to the availability of SiO_2 through early Opx alteration and/or the
670 infiltration of external fluid plausibly sourced from the underlying Centuri gneiss (Fig. 11b). External
671 metamorphic fluids are necessary to explain the Monte Maggiore serpentinization front, as (i) no
672 major internal fluid source was present in the fresh peridotite domains, and (ii) bulk-rock major
673 element results suggest a SiO_2 enrichment in the serpentinized domain. Nevertheless, for at least some
674 serpentine generations, fluids may have also been provided by partial dehydration during lizardite-
675 to-antigorite transformation (see also Debret *et al.*, 2013b), suggesting multiple pathways of
676 serpentinization in the subduction zone.
677
678 ***5.2 Trace element fingerprints of the Monte Maggiore serpentinization front***
679 Compared to other trace elements, REE are useful to identify the precursor minerals from which
680 serpentine formed (Deschamps *et al.*, 2013), thus also providing information about the preservation
681 of primary minerals with respect to the evolution of fluid-rock interaction events and temperature.
682 For preserved peridotites (0 - 35 vol. % serpentinization), and particularly Liz, Atg1, and Atg2, REE
683 patterns resemble those of replaced primary phases (P-Ol and P-Opx). Instead, for higher
684 serpentinization degrees (35 - 75 vol. % serpentinization), Liz/Atg, Atg2, Atg3, and M-Ol, REE
685 patterns are generally intermediate between P-Ol and P-Opx compositions. This may suggest a
686 contemporaneous consumption of both P-Ol and P-Opx during serpentinization, due to increasing
687 fluid/rock ratios, and potentially higher T conditions. In fact, orthopyroxene breakdown during
688 serpentinization is favoured at high-T conditions (>400 °C) (Oelkers and Schott, 2001; Allen and
689 Seyfried, 2003), which are consistent with antigorite stability in subduction zones. We thus suggest
690 that antigorite formation due to early P-Opx consumption (Figs. 4c, d) characterizes partially

691 serpentinized peridotites (>35 vol. % serpentinization). In less serpentinized rocks, low fluid/rock
692 (F/R) ratios and a_{SiO2} may have not been high enough to stabilize antigorite, leading to the formation
693 of dominant lizardite. This latter interpretation is consistent with the chemical variation scenario
694 proposed in section 5.1 which involves a SiO_2 input from external fluid(s) (Fig. 11b).

695 Available *in situ* trace element data (Debret, 2013) in partially serpentinized peridotites from
696 the Monte Maggiore massif evidence a decrease in REE contents from early lizardite veins (V1 in
697 Debret, 2013) with patterns similar to those of Opx, to late lizardite veins (V2 and V3 in Debret,
698 2013), with patterns intermediate between those of P-Ol and P-Opx. This geochemical variation was
699 interpreted as evidence of decreasing T conditions during oceanic serpentinization (Debret, 2013).
700 Our geochemical results, coupled with identified serpentine generations across varying
701 serpentinization degrees, provide a complementary point of view. In serpentinites (75 – 100 vol. %),
702 Liz/Atg, Atg3, and Atg4 are more enriched in LREE compared to preserved and partially
703 serpentinized peridotites. This reflects a redistribution of the least fluid-mobile elements among these
704 three main primary mantle phases (P-Ol, P-Opx, P-Cpx).

705 A salient aspect related to the timing of serpentinization, is the source of fluid(s). *In situ* FME
706 characterization may provide insight into specific microstructural domains related to serpentinization.
707 Previous studies have evidenced that different serpentine generations, often corresponding to
708 different serpentine polysomes, display significant variations in FME concentrations. For example,
709 in mantle wedge serpentinites from Tso Morari (Himalaya), Deschamps *et al.* (2010) highlighted
710 differences in enrichment of several FME such as Li, B, As, Sb, Cs, Ba, Pb, and U between two
711 distinct serpentinization episodes occurring at different T and environments in subduction zone
712 setting. Similarly, Peters *et al.* (2017), showed that alkalis-to-U elemental ratios and FME can be
713 diagnostic of forearc *vs.* mid-ocean ridge serpentinization environments. This feature clearly emerges
714 from the study of several subducted segments of former oceanic lithosphere showing alkali-to-U
715 elemental ratios, and FME patterns similar to forearc serpentinites.

716 Previous studies also investigated the behaviour of FME during prograde subduction
717 metamorphic paths involving fluid loss associated with serpentine recrystallization (*e.g.*, Scambelluri
718 *et al.*, 2004; Vils *et al.*, 2011; Kodolányi and Pettke, 2011; Deschamps *et al.*, 2012; Lafay *et al.*, 2013;
719 Cannaò and Debret, 2024). These studies evidence variable (minor to major) loss of FME elements
720 from low-T to high-T polysomes, especially Li, B, and in some cases Sr and Cs. However, these
721 studies were conducted on samples from different tectono-metamorphic units and localities, which
722 may result in inherited variability in FME compositions (Martin *et al.*, 2020). Nevertheless, a decrease
723 in B and Sr was also observed by Kodolányi and Pettke, (2011) when comparing chrysotile (LT) and
724 antigorite (HT) from the same samples. Furthermore, the modifications in FME concentrations may
725 not only be attributed to serpentine phase transitions. For instance, in the Voltri Massif (Ligurian
726 Western Alps, Italy) a reset in FME concentrations, together with increasing in $^{87}Sr/^{86}Sr$ ratios, from
727 static to mylonitic serpentinites evidenced the contribution of external fluids circulating and
728 interacting within deformed domains (Cannaò *et al.*, 2016). Debret *et al.*, (2013b) investigated
729 eclogite-facies serpentinites from the Lanzo ultramafic massif (Western Italian Alps), as an example
730 of subducted oceanic lithosphere that recorded multiple serpentinization/deserpentinization events.
731 This study evidenced a decrease in Li, B, As, and Ba between lizardite and antigorite during prograde
732 metamorphism, and additional loss of B, Sb, Ba, and Rb associated with metamorphic olivine growth.
733 The loss of FME especially concerns foliated serpentinites affected by fluid circulation.
734 In this study we compared the different serpentine generations from the Monte Maggiore
735 massif as representative of different serpentinization steps across a serpentinization front. In contrast
736 with previous works, in partially serpentinized samples (<75 vol. % serpentinization) of the Monte
737 Maggiore massif, the LT polysome Liz is depleted in B, Sr, Cs, and Ba compared to the subsequent
738 high-T antigorite or mixed lizardite-antigorite generations, being the latter related to either
739 replacement of previous serpentine generations (Liz/Atg, Atg1, Atg3) or replacement of primary
740 mantle minerals (Atg2). The only exception is Rb, which is more enriched in Liz relative to other

741 serpentine generations (Fig. 10). No systematic differences were observed in antigorite-dominated
742 generations, which show variable trends of enrichment/depletion in FMEs.

743 Despite the possible contamination of minute serpentine crystals in the LA-ICP-MS analyses
744 of M-Ol, the higher concentration of Li, Sr and Ba suggest actual enrichment in these elements in M-
745 Ol compared to serpentine minerals (Fig. 10). This enrichment may suggest the involvement of an
746 external fluid during growth of M-Ol, or the preferential incorporation of Li, Sr and Ba in M-Ol
747 compared to metamorphic fluids (see Tenthorey and Hermann, 2004; Scambelluri *et al.*, 2019),
748 modulating their release in subduction.

749 Serpentine generations in serpentinites (serpentinization degree >75 vol. %) are overall more enriched
750 in most FMEs compared to the same generations in preserved and partially serpentinized peridotites
751 (<75 vol. % serpentinization), with the only exception of Li and Pb which are less enriched in
752 serpentinites (Fig. 10). This latter trend may highlight the fluid-mobile nature of these elements in
753 serpentine during fluid-rock interactions, and therefore their tendency to be retained in the fluid (see
754 Tenthorey and Hermann, 2004).

755 Results from Monte Maggiore are therefore compared with other localities for which trace
756 element characterizations across serpentinization fronts are available and from two different
757 serpentinization settings (Fig. 12): the Semail ophiolite (Oman), where the serpentinization front
758 testifies the infiltration of slab-derived fluids into the overlying mantle wedge (Prigent *et al.*, 2018),
759 and the Lanzo Massif (Westen Italian Alps), which is interpreted as a fragment of subducted oceanic
760 mantle characterized by an inherited oceanic serpentinization front propagating from the boundary of
761 the massif towards its fresh peridotite core (Boudier, 1978; Lagabrielle *et al.*, 1990; Kaczmarek and
762 Müntener, 2008; Debret *et al.*, 2013a; Debret *et al.*, 2013b). Selected data from Monte Maggiore, the
763 Semail ophiolite, and Lanzo are compared in Figure 12 as a function of the relative distance within
764 the main serpentinization front and serpentinization degree. Serpentinization fronts from Monte
765 Maggiore and the Semail ophiolite share similar trends for B, Sr, and Ba, displaying decreasing
766 concentrations with the increasing distance from the boundary of the serpentinization front (and

767 decreasing serpentinization degree in Monte Maggiore). In contrast, Lanzo shows an opposite trend
768 with FME increasing from the boundary of the massif towards the inner part of the serpentinization
769 front and for decreasing serpentinization degrees. Lithium, instead, shows a similar behaviour among
770 the three localities, decreasing its concentration in serpentinites at the boundary with oceanic
771 sediments. The similarity in FME patterns between Monte Maggiore and the Semail ophiolite may
772 be explained by the infiltration of metamorphic fluids from the base of the serpentinization front –
773 *i.e.*, the tectonic contact with Centuri at Monte Maggiore, and the plate interface for the Semail
774 ophiolite – during subduction. The Lanzo serpentinites, instead, are interpreted as subducted
775 serpentinites that partially lost FMEs during progressive mineral phase transformations in subduction
776 (from lizardite to antigorite) and infiltration of metamorphic fluids in the subduction zone (Debret *et*
777 *al.*, 2013b). Similar conditions are also documented in Monte Maggiore, with serpentine transitions
778 from lizardite to antigorite to metamorphic olivine. It is therefore possible that the FME profile in
779 Lanzo still reflects inherited oceanic serpentinization patterns. This hypothesis cannot be currently
780 tested owing to the lack of *in situ* FME data across oceanic serpentinization profiles.

781 Although large uncertainty still exists on the interpretation of the origin of fluids involved in
782 serpentinization and timing of this process, especially in subducted sections of oceanic lithosphere
783 like Monte Maggiore and Lanzo, the collected data and comparisons to other case studies suggest that
784 Monte Maggiore shares similar FME patterns with a subduction-related serpentinization front such
785 as the Semail ophiolite. This similarity is supported by the geological setting of the Monte Maggiore
786 massif, indicating the development of the main serpentinization front from the underlying tectonic
787 contact with the Centuri gneiss. The fluid-rock evolution of Lanzo is probably more articulated and
788 characterized by the overprinting of serpentinization stages occurred at the oceanic stage, by the
789 successive fluid-rock interactions and deformation during subduction, as suggested by Debret *et al.*
790 (2013b). This comparison is summarized in the sketch of Figure 13, which highlights the potentially
791 distinctive chemical features of subduction-zone serpentinization fronts relative to inherited oceanic
792 serpentinization fronts suggested by the collected dataset.

If confirmed by future studies, especially addressing oceanic serpentinization fronts, the analyses of FME profiles across serpentinization fronts will prove as a valuable approach to infer the setting of serpentinization in orogenic serpentinites, where other distinguishing factors of ocean floor *vs.* subduction-related serpentinization may not be available. From the present work, it also emerges that the study of serpentinization processes strongly benefits form the consideration of mineralogical and chemical variations across continuous serpentinization fronts. Evolutionary stages resulting from the comparison of isolated samples with variably serpentinized degree, instead, may result in inaccurate assumptions. For example, least serpentinized samples do not necessarily reflect the early stages of serpentinization, but rather more evolved ones marking the end of the serpentinization front.

Based on the collected data and on our interpretations, Monte Maggiore may represent an example of fossilized tectonic boundary similar to a slab-forearc mantle wedge interface (*i.e.*, Centuri gneiss-Monte Maggiore interface). Its structural position within the Alpine Corsica metamorphic stack (Vitale Brovarone *et al.*, 2013) may be consistent with such a hypothesis. Similar interpretations are suggested for the tectonic evolution of the Erro-Tobbio ultramafic unit, Western Italian Alps, which is interpreted as a fragment of subducted oceanic lithosphere that, during its Alpine orogenic evolution, was flushed by fluids sourced from the underlying subducting oceanic units (Fruh-Green *et al.*, 2001; Scambelluri and Tonarini, 2012). In both Monte Maggiore and Erro Tobbio, this mantle wedge-like position and the preservation of large portions of fresh mantle assemblages during subduction (Rampone *et al.*, 2008; Piccardo and Guarnieri 2010) represent the ideal conditions to promote subduction serpentinization by metamorphic fluids. The chemical features described in the present study may therefore represent a proxy for the chemical fingerprints of subduction zone serpentinization fronts.

5.3 Serpentinization of Monte Maggiore and the generation of reduced metamorphic fluids

The reconstructed serpentinization history supports the formation of several serpentine generations at the expense of primary or metamorphic olivine during the metamorphic evolution of the Monte

Maggiore body during Alpine subduction zone. The transition zone from partially serpentinized peridotites to serpentinites provides the constraint that a significant proportion of serpentine in these rocks is antigorite that formed directly at the expense of primary mantle minerals, as supported by microstructural relationships. This indicates that a substantial fraction of serpentinization occurred likely in the Alpine subduction zone. The release of reduced fluids associated with serpentinization have long been identified at subseafloor conditions and on land in ophiolitic massifs (Kelley *et al.*, 2005; Marcaillou *et al.*, 2011; Andreani *et al.*, 2013; Klein *et al.*, 2014). More recently, the role of serpentinization in the production of natural energy sources such as H_2 and CH_4 has also been discussed in subduction zones (Vitale Brovarone *et al.*, 2020; Boutier *et al.*, 2021; Boutier *et al.*, 2024). Previous works interpret the serpentinization of Monte Maggiore as the result of seawater-peridotite interactions (Debret, 2013; Debret *et al.*, 2014). This interpretation implies that, if serpentinization took place at the ocean floor, the production of reduced fluids during olivine to magnetite reactions in the serpentinized domains of Monte Maggiore was exhausted at subseafloor conditions. However, the new interpretation proposed in this study, pointing serpentinization occurring dominantly during subduction, may imply the release of such reduced fluids at much greater depths in the Alpine subduction zone.

Bulk rock analyses display increasing Fe_2O_3/Fe_{tot} ratios for increasing serpentinization degrees (Fig. 7d). This partial Fe oxidation is also testified by the presence of magnetite in all identified serpentine generations, but in different proportions. For example, Liz, Atg1 and Atg2 are generally associated with smaller magnetite amounts relative to the other generations. Alternatively, serpentine may have acted as a sink for ferric iron. *In situ* Fe valence measurements are available for fully serpentinized rock in Monte Maggiore, for which serpentinization conditions are not robustly constrained, and show Fe^{3+}/Fe_{tot} values similar to oceanic or low-temperature equivalents (Debret *et al.*, 2014). However, the lack of detailed studies of *in situ* Fe valence patterns in serpentine generations in partially serpentinized peridotites from the Monte Maggiore massif makes robust assessments on the redox potential of the documented subduction serpentinization events challenging.

6. CONCLUSIONS

Through a field-based and high-spatial resolution sampling approach, we characterized the serpentinization history and chemical compositions across a serpentinization front of a subducted peridotite body. Our study suggests that the Monte Maggiore massif serpentinization front recorded fluid circulation along a subduction-zone tectonic contact. Successive serpentine generations are present across the serpentinization front and their distribution is consistent throughout the massif: lizardite is preserved in the inner, less serpentinized portion, where low fluid influx and negligible SiO_2 gain for antigorite formation were available. Widespread antigorite is prevailing in more serpentinized domains towards the basal tectonic contact, replacing previous serpentine generations and primary mantle minerals. Bulk rock major elements evidenced a SiO_2 increase with increasing serpentinization, suggesting that serpentinization occurred in an open system with input of silica-rich metamorphic fluids from, most plausibly, the underlying Centuri continental unit. This chemical gradient also favours the hypothesis of a subduction-related serpentinization front rather than an inherited oceanic equivalent. Concentrations of FME from preserved to partially serpentinized peridotites (0 – 75 vol. %) show minor differences among serpentine generations, with a slight gain in the majority of FME at the Liz to Atg transition. Fluid-mobile element concentrations increase with increasing serpentinization degree towards the basal tectonic contact, and this is explained by the infiltration of metamorphic fluids during subduction. Such FME patterns across the Monte Maggiore serpentinization front are similar to those described across the serpentinization front at the base of the forearc mantle wedge serpentinites from the Semail ophiolite, Oman, and opposite to subducted oceanic serpentinites from Lanzo Massif, western Alps. The Monte Maggiore FME distribution acquired from the upward migration of serpentinizing fluids is therefore preserved and might be diagnostic of such type of environments in subduction zones.

AKNOWLEDGMENTS

This work is part of a project funded by the European Research Council (ERC) under the European Union's Horizon 2020 research and innovation program (Grant agreement No. 864045; project acronym DeepSeep). A MIUR Rita Levi Montalcini grant, a MUR FARE grant (No. R20ZIYMPAR; acronym DRYNK), and a MUR PRIN2022 grant (No. 20224YR3AZ; acronym HYDECARB) to Alberto Vitale Brovarone, and the NFR 324301 to Zeudia Pastore are also acknowledged. We acknowledge Gianluca Sessa, at the Geochemistry, Geochronology and Isotope Geology laboratory (University of Milan), for technical support during LA-ICP-MS sessions. We also acknowledge Francesco Giuntoli and Guillaume Siron for assistance during fieldwork and discussions.

BIBLIOGRAPHY

Allen, D. E., and Seyfried, W. E. (2003). Compositional controls on vent fluids from ultramafic-hosted hydrothermal systems at mid-ocean ridges: An experimental study at 400°C, 500 bars. *Geochimica et Cosmochimica Acta*, *67*(8), 1531–1542. https://doi.org/10.1016/S0016-7037(02)01173-0

Andreani, M., Mével, C., Boullier, A. M., and Escartín, J. (2009). LA-(HR-) ICPMS study of serpentinites from ODP Site 920 (23°N MAR): insights on transfers and trace element distribution during serpentinization. *EGUGA*, *8*(2), 13248. https://doi.org/10.1029/2006GC001373

Andreani, M., Muñoz, M., Marcaillou, C., and Delacour, A. (2013). µXANES study of iron redox state in serpentine during oceanic serpentinization. *Lithos*, *178*, 70–83. https://doi.org/10.1016/j.lithos.2013.04.008

Auzende, A. L., Daniel, I., Reynard, B., Lemaire, C., & Guyot, F. (2004). High-pressure behaviour of serpentine minerals: a Raman spectroscopic study. *Physics and Chemistry of Minerals*, *31*, 269-277. https://doi.org/10.1007/s00269-004-0384-0

892 Basch, V., Rampone, E., Crispini, L., Ferrando, C., Ildefonse, B., and Godard, M. (2018). From
893 mantle peridotites to hybrid troctolites: Textural and chemical evolution during melt-rock
894 interaction history (Mt. Maggiore, Corsica, Fance). *Lithos*, *323*, 4–23.
895 https://doi.org/10.1016/j.lithos.2018.02.025
896 Beltrando, M., Manatschal, G., Mohn, G., Dal Piaz, G. V., Brovarone, A. V., & Masini, E. (2014).
897 Recognizing remnants of magma-poor rifted margins in high-pressure orogenic belts: The
898 Alpine case study. *Earth-Science Reviews*, *131*, 88-115.
899 https://doi.org/10.1016/j.earscirev.2014.01.001
900 Bostock, M. G., Hyndman, R. D., Rondenay, S., and Peacock, S. M. (2002). An inverted continental
901 Moho and serpentinization of the forearc mantle. *Nature*, *417*(6888), 536-538.
902 https://doi.org/10.1038/417536a
903 Boudier, F. (1978). Structure and petrology of the Lanzo peridotite massif (Piedmont Alps).
904 *Geological Society of America Bulletin*, *89*(10), 1574-1591.
905 Boutier, A., Martinez, I., Sissmann, O., Agostini, S., Daniel, I., Van Baalen, M., Mana, S., and Vitale
906 Brovarone, A. (2024). Complexity of graphite formation in response to metamorphic methane
907 generation and transformation in an orogenic ultramafic body. *Geochimica et Cosmochimica*
908 *Acta*, *364*, 166–183. https://doi.org/10.1016/J.GCA.2023.10.028
909 Boutier, A., Vitale Brovarone, A., Martinez, I., Sissmann, O., and Mana, S. (2021). High-pressure
910 serpentinization and abiotic methane formation in metaperidotite from the Appalachian
911 subduction, northern Vermont. *Lithos*, *396–397*. https://doi.org/10.1016/j.lithos.2021.106190
912 Cannaò, E., & Debret, B. (2024). Variable δ11B signatures reflect dynamic evolution of the Mariana
913 serpentinite forearc. *Geochemical Perspectives Letters*, *30*, 13-19.
914 https://doi.org/10.7185/geochemlet.2416
915 Cannaò, E., Scambelluri, M., Agostini, S., Tonarini, S., and Godard, M. (2016). Linking serpentinite
916 geochemistry with tectonic evolution at the subduction plate-interface: The Voltri Massif case

study (Ligurian Western Alps, Italy). *Geochimica et Cosmochimica Acta*, *190*, 115-133. https://doi.org/10.1016/j.gca.2016.06.034

Caruso, L. J., and Joseph Chernosky, eNo V. (1979). The stabitity of lizardite. *Can. Mineral*, *17*(4), 757_769.

Compagnoni, R., Cossio, R., and Mellini, M. (2021). Raman anisotropy in serpentine minerals, with a caveat on identification. *Journal of Raman Spectroscopy*, *52*(7), 1334–1345. https://doi.org/10.1002/JRS.6128

Dandar, O., Okamoto, A., Uno, M., Oyanagi, R., Nagaya, T., Burenjargal, U., Miyamoto, T., and Tsuchiya, N. (2019). Formation of secondary olivine after orthopyroxene during hydration of mantle wedge: evidence from the Khantaishir Ophiolite, western Mongolia. *Contributions to Mineralogy and Petrology*, *174*(11). https://doi.org/10.1007/s00410-019-1623-1

Debret B. (2013). Serpentinites, vecteurs des circulations uides et des transferts chimiques de l'oc_eanisation _a la subduction : exemple dans les Alpes occidentales. *Sciences de la Terre. Universit_e Blaise Pascal - Clermont-Ferrand II*. Fran_cais. <NNT : 2013CLF22389> <tel-01037950>

Debret, B., Andreani, M., Godard, M., Nicollet, C., Schwartz, S., and Lafay, R. (2013b). Trace element behavior during serpentinization/de-serpentinization of an eclogitized oceanic lithosphere: A LA-ICPMS study of the Lanzo ultramafic massif (Western Alps). *Chemical Geology*, *357*, 117–133. https://doi.org/10.1016/j.chemgeo.2013.08.025

Debret, B., Andreani, M., Muñoz, M., Bolfan-Casanova, N., Carlut, J., Nicollet, C., Schwartz, S., and Trcera, N. (2014). Evolution of Fe redox state in serpentine during subduction. *Earth and Planetary Science Letters*, *400*, 206–218. https://doi.org/10.1016/j.epsl.2014.05.038

Debret, B., Nicollet, C., Andreani, M., Schwartz, S., and Godard, M. (2013a). Three steps of serpentinization in an eclogitized oceanic serpentinization front (Lanzo Massif - Western Alps). *Journal of Metamorphic Geology*, *31*(2), 165–186. https://doi.org/10.1111/jmg.12008

942 Delacour, A., Früh-Green, G. L., and Bernasconi, S. M. (2008). Sulfur mineralogy and geochemistry
943 of serpentinites and gabbros of the Atlantis Massif (IODP Site U1309). *Geochimica et*
944 *Cosmochimica Acta*, *72*(20), 5111–5127. https://doi.org/10.1016/J.GCA.2008.07.018
945 Deschamps, F., Godard, M., Guillot, S., and Hattori, K. (2013). Geochemistry of subduction zone
946 serpentinites: A review. *Lithos*, *178*, 96-127. https://doi.org/10.1016/j.lithos.2013.05.019
947 Deschamps, F., Godard, M., Guillot, S., Chauvel, C., Andreani, M., Hattori, K., Wunder, B., and
948 France, L. (2012). Behavior of fluid-mobile elements in serpentines from abyssal to subduction
949 environments: Examples from Cuba and Dominican Republic. *Chemical Geology*, *312–313*, 93–
950 117. https://doi.org/10.1016/j.chemgeo.2012.04.009
951 Deschamps, F., Guillot, S., Godard, M., Chauvel, C., Andreani, M., and Hattori, K. (2010). *In situ*
952 characterization of serpentinites from forearc mantle wedges: Timing of serpentinization and
953 behavior of fluid-mobile elements in subduction zones. *Chemical Geology*, *269*(3–4), 262–277.
954 https://doi.org/10.1016/j.chemgeo.2009.10.002
955 Durand-Delga, M., (1978). Corse. Guides géologiques régionaux, *Masson, Paris. 208 pp.*
956 Durand-Delga, M., (1984). Principaux traits de la Corse Alpine et corrélations avec les
957 Alpes Ligures. *Memorie della Società Geologica Italiana 28, 285–329.*
958 Etiope, G., and Sherwood Lollar, B. (2013). Abiotic methane on earth. *Reviews of Geophysics*, *51*(2),
959 276–299. https://doi.org/10.1002/ROG.20011
960 Evans, B. W. (2004). The Serpentinite Multisystem Revisited: Chrysotile Is Metastable. *International*
961 *Geology Review*, *46*(6), 479–506. https://doi.org/10.2747/0020-6814.46.6.479
962 Evans, B. W., Hattori, K., and Baronnet, A. (2013). Serpentinite: what, why, where?. *Elements*, *9*(2),
963 99-106. https://doi.org/10.2113/gselements.9.2.99
964 Fabbri, O., Magott, R., Fournier, M., and Etienne, L. (2018). Pseudotachylyte in the Monte Maggiore
965 ophiolitic unit (Alpine Corsica): A possible lateral extension of the Cima di Gratera
966 intermediate-depth Wadati-Benioff paleo-seismic zone. *BSGF - Earth Sciences Bulletin*, *189*(4–
967 6). https://doi.org/10.1051/bsgf/2018020

968 Früh-Green, G. L., Scambelluri, M., and Vallis, F. (2001). O–H isotope ratios of high pressure
969 ultramafic rocks: implications for fluid sources and mobility in the subducted hydrous mantle.
970 *Contributions to Mineralogy and Petrology*, *141*(2), 145-159.
971 https://doi.org/10.1007/s004100000228
972 Griffin, W. L. (2008). GLITTER: data reduction software for laser ablation ICP-MS. *Laser Ablation*
973 *ICP-MS in the Earth Sciences: Current practices and outstanding issues*, 308-311.
974 Groppo, C., Rinaudo, C., Cairo, S., Gastaldi, D., & Compagnoni, R. (2006). Micro-Raman
975 spectroscopy for a quick and reliable identification of serpentine minerals from ultramafics.
976 *European Journal of Mineralogy*, *18*(3), 319-329. https://doi.org/10.1127/0935-
977 1221/2006/0018-0319
978 Guillot, S., Schwartz, S., Reynard, B., Agard, P., and Prigent, C. (2015). Tectonic significance of
979 serpentinites. *Tectonophysics*, *646*, 1–19. https://doi.org/10.1016/J.TECTO.2015.01.020
980 Hart, S. R., and Zindler, A. (1986). In search of a bulk-Earth composition. *Chemical Geology*, *57*(3-
981 4), 247-267. https://doi.org/10.1016/j.tecto.2015.01.020
982 Hattori, K. H., and Guillot, S. (2007). Geochemical character of serpentinites associated with high-to
983 ultrahigh-pressure metamorphic rocks in the Alps, Cuba, and the Himalayas: Recycling of
984 elements in subduction zones. *Geochemistry, Geophysics, Geosystems*, *8*(9).
985 https://doi.org/10.1029/2007GC001594
986 Heiri, O., Lotter, A. F., and Lemcke, G. (2001). Loss on ignition as a method for estimating organic
987 and carbonate content in sediments: Reproducibility and comparability of results. *Journal of*
988 *Paleolimnology*, *25*(1), 101–110. https://doi.org/10.1023/A:1008119611481/METRICS
989 Holt, A. F., and Condit, C. B. (2021). Slab Temperature Evolution Over the Lifetime of a Subduction
990 Zone. *Geochemistry, Geophysics, Geosystems*, *22*(6), e2020GC009476.
991 https://doi.org/10.1029/2020GC009476
992 Hyndman, R. D., and Peacock, S. M. (2003). Serpentinization of the forearc mantle. *Earth and*
993 *Planetary Science Letters*, *212*(3-4), 417-432. https://doi.org/10.1038/417536a

994 Jackson, M. D., Ohnenstetter, M. (1981). Peridotite and Gabbroic Structures in the peridotite and
995 gabbroic structures in the Monte Maggiore massif, Alpine Corsica. *The Journal of Geology*,
996 *89*(6). https://doi.org/10.1086/628637
997 Jagoutz, E., Palme, H., Baddenhausen, H., Blum, K., Cendales, M., Dreibus, G., ... and Wänke, H.
998 (1979). The abundances of major, minor and trace elements in the earth's mantle as derived from
999 primitive ultramafic nodules. In: *Lunar and Planetary Science Conference, 10th, Houston, Tex.,*
1000 *March 19-23, 1979, Proceedings. Volume 2. (A80-23617 08-91) New York, Pergamon Press,*
1001 *Inc., 1979, p. 2031-2050. Research supported by the Deutsche Forschungsgemeinschaft.* (Vol.
1002 10, pp. 2031-2050).
1003 Jolivet, L., Faccenna, C., Goffé, B., Mattei, M., Rossetti, F., Brunet, C., ... and Parra, T. (1998).
1004 Midcrustal shear zones in postorogenic extension: example from the northern Tyrrhenian Sea.
1005 *Journal of Geophysical Research: Solid Earth*, *103*(B6), 12123-12160.
1006 https://doi.org/10.1029/97JB03616
1007 Kaczmarek, M. A., and Müntener, O. (2008). Juxtaposition of Melt Impregnation and High-
1008 Temperature Shear Zones in the Upper Mantle; Field and Petrological Constraints from the
1009 Lanzo Peridotite (Northern Italy). *Journal of Petrology*, *49*(12), 2187–2220.
1010 https://doi.org/10.1093/PETROLOGY/EGN065
1011 Kelemen, P. B., Dick, H. J., and Quick, J. E. (1992). Formation of harzburgite by pervasive melt/rock
1012 reaction in the upper mantle. *Nature*, *358*(6388), 635-641.
1013 Kelley, D. S., Karson, J. A., Früh-Green, G. L., Yoerger, D. R., Shank, T. M., Butterfield, D. A.,
1014 Hayes, J. M., Schrenk, M. O., Olson, E. J., Proskurowski, G., Jakuba, M., Bradley, A., Larson,
1015 B., Ludwig, K., Glickson, D., Buckman, K., Bradley, A. S., Brazelton, W. J., Roe, K., … Sylva,
1016 S. P. (2005). A serpentinite-hosted ecosystem: The Lost City hydrothermal field. *Science*,
1017 *307*(5714), 1428–1434.
1018 https://doi.org/10.1126/SCIENCE.1102556/SUPPL_FILE/KELLEY.SOM.PDF

1019 Klein, F., Bach, W., Humphris, S. E., Kahl, W. A., Jöns, N., Moskowitz, B., and Berquó, T. S. (2014).
1020 Magnetite in seafloor serpentinite—Some like it hot. *Geology*, *42*(2), 135-138.
1021 https://doi.org/10.1130/G35068.1
1022 Kodolányi, J., and Pettke, T. (2011). Loss of trace elements from serpentinites during fluid-assisted
1023 transformation of chrysotile to antigorite—An example from Guatemala. *Chemical Geology*,
1024 *284*(3-4), 351-362. https://doi.org/10.1016/j.chemgeo.2011.03.016
1025 Kodolányi, J., Pettke, T., Spandler, C., Kamber, B. S., and Gméling, K. (2012). Geochemistry of
1026 ocean floor and fore-arc serpentinites: constraints on the ultramafic input to subduction zones.
1027 *Journal of Petrology*, *53*(2), 235-270. https://doi.org/10.1093/petrology/egr058
1028 Lafay, R., Deschamps, F., Schwartz, S., Guillot, S., Godard, M., Debret, B., and Nicollet, C. (2013).
1029 High-pressure serpentinites, a trap-and-release system controlled by metamorphic conditions:
1030 Example from the Piedmont zone of the western Alps. *Chemical Geology*, *343*, 38–54.
1031 https://doi.org/10.1016/j.chemgeo.2013.02.008
1032 Lagabrielle, Y., and Cannat, M. (1990). Alpine Jurassic ophiolites resemble the modern central
1033 Atlantic basement. *Geology*, *18*(4), 319-322. https://doi.org/10.1130/0091-
1034 7613(1990)018<0319:AJORTM>2.3.CO;2
1035 Lagabrielle, Y., Brovarone, A. V., and Ildefonse, B. (2015). Fossil oceanic core complexes
1036 recognized in the blueschist metaophiolites of Western Alps and Corsica. *Earth-Science*
1037 *Reviews*, *141*, 1-26. https://doi.org/10.1016/j.earscirev.2014.11.004
1038 Lagabrielle, Y., Fudral, S., and Kienast, J. R. (1990). La couverture océanique des ultrabasites de
1039 Lanzo (Alpes occidentales): arguments lithostratigraphiques et pétrologiques. *Geodinamica*
1040 *Acta*, *4*(1), 43–55. https://doi.org/10.1080/09853111.1990.11105199
1041 Lahondère, D., and Guerrot, C. (1997). Datation SM-Nd du métamorphisme éclogitique en Corse
1042 alpine : un argument pour l'existence au Crétacé supérieur d'une zone de subduction active
1043 localisée sous le bloc corso-sarde. *Géologie de La France*, *3*, 3–11.

1044 Lahondère, D., (1996). Les schistes blues et les éclogites à lawsonite des unites
1045 continentales et océanique de la Corse alpine. Nouvelles donnée pétrologique et
1046 structurales (Corse). *Documents du BRGM. 240 pp.*
1047 Magott, R., Fabbri, O., and Fournier, M. (2020). Seismically-induced serpentine dehydration as a
1048 possible mechanism of water release in subduction zones. Insights from the Alpine Corsica
1049 pseudotachylyte-bearing Monte Maggiore ophiolitic unit. *Lithos*, *362–363*.
1050 https://doi.org/10.1016/j.lithos.2020.105474
1051 Malavieille J. (1983). Etude tectonique et microtectonique de la nappe de socle de Centuri (zone des
1052 schistes lustres de Corse); Consequences pour la geometrie de la chaine alpine. *Bulletin de la*
1053 *Société Géologique de France, S7-XXV (2): 195–204*. doi: https://doi.org/10.2113/gssgfbull.S7-
1054 XXV.2.195
1055 Malavieille, Chemenda, and Larroque. (1998). Evolutionary model for Alpine Corsica: Mechanism
1056 for ophiolite emplacement and exhumation of high-pressure rocks. *Terra Nova*, *10*(6), 317-322.
1057 https://doi.org/10.1046/j.1365-3121.1998.00208.x
1058 Malvoisin, B. (2015). Mass transfer in the oceanic lithosphere: Serpentinization is not isochemical.
1059 *Earth and Planetary Science Letters*, *430*, 75–85. https://doi.org/10.1016/J.EPSL.2015.07.043
1060 Marcaillou, C., Muñoz, M., Vidal, O., Parra, T., and Harfouche, M. (2011). Mineralogical evidence
1061 for H2 degassing during serpentinization at 300 °C/300 bar. *Earth and Planetary Science*
1062 *Letters*, *303*(3–4). 281–290. https://doi.org/10.1016/J.EPSL.2011.01.006
1063 Martin, B., and Fyfe, W. S. (1970). Some experimental and theoretical observations on the kinetics
1064 of hydration reactions with particular reference to serpentinization. *Chemical Geology*, *6*(C),
1065 185–202. https://doi.org/10.1016/0009-2541(70)90018-5
1066 Martin, C., Flores, K. E., Vitale-Brovarone, A., Angiboust, S., and Harlow, G. E. (2020). Deep mantle
1067 serpentinization in subduction zones: Insight from in situ B isotopes in slab and mantle wedge
1068 serpentinites. *Chemical Geology*, *545*, 119637. https://doi.org/10.1016/j.chemgeo.2020.119637

1069 Martin, L. A. J., Rubatto, D., Vitale Brovarone, A., and Hermann, J. (2011). Late Eocene lawsonite-
1070 eclogite facies metasomatism of a granulite sliver associated to ophiolites in Alpine Corsica.
1071 *Lithos*, *125*(1–2), 620–640. https://doi.org/10.1016/J.LITHOS.2011.03.015
1072 Mattauer, M., Faure, M., and Malavieille, J. (1981). Transverse lineation and large-scale structures
1073 related to Alpine obduction in Corsica. *Journal of Structural Geology*, *3*(4), 401–409.
1074 https://doi.org/10.1016/0191-8141(81)90040-7
1075 Moody, J. B. (1976). Serpentinization: a review. *Lithos*, *9*(2), 125-138.
1076 Molli, G., and Malavieille, J. (2011). Orogenic processes and the Corsica/Apennines geodynamic
1077 evolution: insights from Taiwan. *International Journal of Earth Sciences*, *100*, 1207-1224.
1078 https://doi.org/10.1007/s00531-010-0598-y
1079 Nakatani, T., and Nakamura, M. (2016). Experimental constraints on the serpentinization rate of fore-
1080 arc peridotites: Implications for the upwelling condition of the slab-derived fluid. *Geochemistry,*
1081 *Geophysics, Geosystems*, *17*(8), 3393–3419. https://doi.org/10.1002/2016GC006295
1082 Nozaka, T. (2005). Metamorphic history of serpentinite mylonites from the Happo ultramafic
1083 complex, central Japan. *Journal of Metamorphic Geology*, *23*(8), 711–723.
1084 https://doi.org/10.1111/j.1525-1314.2005.00605.x
1085 Oelkers, E. H., and Schott, J. (2001). An experimental study of enstatite dissolution rates as a function
1086 of pH, temperature, and aqueous Mg and Si concentration, and the mechanism of
1087 pyroxene/pyroxenoid dissolution. *Geochimica et Cosmochimica Acta*, *65*(8), 1219–1231.
1088 https://doi.org/10.1016/S0016-7037(00)00564-0
1089 Padrón-Navarta, J. A., Sánchez-Vizcaíno, V. L., Hermann, J., Connolly, J. A. D., Garrido, C. J.,
1090 Gómez-Pugnaire, M. T., and Marchesi, C. (2013). Tschermak's substitution in antigorite and
1091 consequences for phase relations and water liberation in high-grade serpentinites. *Lithos*, *178*,
1092 186–196. https://doi.org/10.1016/J.LITHOS.2013.02.001

1093 Peters, D., Bretscher, A., John, T., Scambelluri, M., and Pettke, T. (2017). Fluid-mobile elements in
1094 serpentinites: Constraints on serpentinisation environments and element cycling in subduction
1095 zones. *Chemical Geology*, *466*, 654–666. https://doi.org/10.1016/j.chemgeo.2017.07.017
1096 Pettke, T., and Bretscher, A. (2022). Fluid-mediated element cycling in subducted oceanic
1097 lithosphere: The orogenic serpentinite perspective. *Earth-science reviews*, *225*, 103896.
1098 https://doi.org/10.1016/j.earscirev.2021.103896
1099 Piccardo, G. B., and Guarnieri, L. (2010). The Monte Maggiore peridotite (Corsica, France): A case
1100 study of mantle evolution in the Ligurian Tethys. *Geological Society Special Publication*, *337*,
1101 7–45. https://doi.org/10.1144/SP337.2
1102 Plümper, O., King, H. E., Geisler, T., Liu, Y., Pabst, S., Savov, I. P., Rost, D., and Zack, T. (2017).
1103 Subduction zone forearc serpentinites as incubators for deep microbial life. *Proceedings of the*
1104 *National Academy of Sciences of the United States of America*, *114*(17), 4324–4329.
1105 https://doi.org/10.1073/pnas.1612147114
1106 Prigent, C., Guillot, S., Agard, P., Lemarchand, D., Soret, M., and Ulrich, M. (2018). Transfer of
1107 subduction fluids into the deforming mantle wedge during nascent subduction: Evidence from
1108 trace elements and boron isotopes (Semail ophiolite, Oman). *Earth and Planetary Science*
1109 *Letters*, *484*, 213-228. https://doi.org/10.1016/j.epsl.2017.12.008
1110 Rampone, E., Hofmann, A. W., and Raczek, I. (2009). Isotopic equilibrium between mantle peridotite
1111 and melt: Evidence from the Corsica ophiolite. *Earth and Planetary Science Letters*, *288*(3–4),
1112 601–610. https://doi.org/10.1016/j.epsl.2009.10.024
1113 Rampone, E., Piccardo, G. B., and Hofmann, A. W. (2008). Multi-stage melt-rock interaction in the
1114 Mt. Maggiore (Corsica, France) ophiolitic peridotites: Microstructural and geochemical
1115 evidence. *Contributions to Mineralogy and Petrology*, *156*(4), 453–475.
1116 https://doi.org/10.1007/s00410-008-0296-y

1117 Ranero, C. R., Phipps Morgan, J., McIntosh, K., and Relchert, C. (2003). Bending-related faulting
1118 and mantle serpentinization at the Middle America trench. *Nature 2003 425:6956*, *425*(6956),
1119 367–373. https://doi.org/10.1038/nature01961
1120 Romairone, A. (1996). Petrologia e geochimica delle peridotiti di Monte Maggiore
1121 (Corsica) (Petrology and geochemistry of the Monte Maggiore peridotites). *Graduate thesis,*
1122 *University of Genova*.
1123 Rossetti, F., Glodny, J., Theye, T., and Maggi, M. (2015). Pressure–temperature–deformation–time
1124 of the ductile Alpine shearing in Corsica: From orogenic construction to collapse. *Lithos*, *218–*
1125 *219*, 99–116. https://doi.org/10.1016/J.LITHOS.2015.01.011
1126 Rouméjon, S., Andreani, M., and Früh-Green, G. L. (2019). Antigorite crystallization during oceanic
1127 retrograde serpentinization of abyssal peridotites. *Contributions to Mineralogy and Petrology*,
1128 *174*(7). https://doi.org/10.1007/s00410-019-1595-1
1129 Scambelluri, M., and Tonarini, S. (2012). Boron isotope evidence for shallow fluid transfer across
1130 subduction zones by serpentinized mantle. *Geology*, *40*(10), 907–910.
1131 https://doi.org/10.1130/G33233.1
1132 Scambelluri, M., Cannaò, E., and Gilio, M. (2019). The water and fluid-mobile element cycles during
1133 serpentinite subduction. A review. *European Journal of Mineralogy*, *31*(3), 405–428.
1134 https://doi.org/10.1127/ejm/2019/0031-2842
1135 Scambelluri, M., Fiebig, J., Malaspina, N., Müntener, O., and Pettke, T. (2004). Serpentinite
1136 Subduction: Implications for Fluid Processes and Trace-Element Recycling. *International*
1137 *Geology Review*, *46*(7), 595–613. https://doi.org/10.2747/0020-6814.46.7.595
1138 Scambelluri, M., Pettke, T., Rampone, E., Godard, M., & Reusser, E. (2014). Petrology and trace
1139 element budgets of high-pressure peridotites indicate subduction dehydration of serpentinized
1140 mantle (Cima di Gagnone, Central Alps, Switzerland). *Journal of Petrology*, *55*(3), 459-498.
1141 https://doi.org/10.1093/petrology/egt068

1142 Schrenk, M. O., Brazelton, W. J., and Lang, S. Q. (2013). Serpentinization, carbon, and deep life.
1143 *Reviews in Mineralogy and Geochemistry*, *75*(1), 575-606.
1144 https://doi.org/10.2138/rmg.2013.75.18
1145 Schwartz, S., Guillot, S., Reynard, B., Lafay, R., Debret, B., Nicollet, C., Lanari, P., and Auzende,
1146 A. L. (2013). Pressure-temperature estimates of the lizardite/antigorite transition in high pressure
1147 serpentinites. *Lithos*, *178*, 197–210. https://doi.org/10.1016/j.lithos.2012.11.023
1148 Sun, S. S., & McDonough, W. F. (1989). Chemical and isotopic systematics of oceanic basalts:
1149 implications for mantle composition and processes. *Geological Society, London, Special*
1150 *Publications*, *42*(1), 313-345. https://doi.org/10.1144/GSL.SP.1989.042.01.19
1151 Syracuse, E. M., van Keken, P. E., Abers, G. A., Suetsugu, D., Bina, C., Inoue, T., Wiens, D., and
1152 Jellinek, M. (2010). The global range of subduction zone thermal models. *Physics of the Earth*
1153 *and Planetary Interiors*, *183*(1–2), 73–90. https://doi.org/10.1016/J.PEPI.2010.02.004
1154 Tenthorey, E., and Hermann, J. (2004). Composition of fluids during serpentinite breakdown in
1155 subduction zones: Evidence for limited boron mobility. *Geology*, *32*(10), 865–868.
1156 https://doi.org/10.1130/G20610.1
1157 Terry, R.D., Chilinger, G.V. (1955). Comparison charts for visual estimation of percent- age
1158 composition. *J. Sediment. Petrol. 25*, 229–234.
1159 Ulmer, P., and Trommsdorff, V. (1995). Serpentine Stability to Mantle Depths and Subduction-
1160 Related Magmatism. *Science*, *268*(5212), 858–861.
1161 https://doi.org/10.1126/SCIENCE.268.5212.858
1162 Vesin, C., Rubatto, D., & Pettke, T. (2024). The history of serpentinisation at mid-ocean ridges:
1163 Insights from in situ trace elements coupled with oxygen and boron isotopes. *Chemical Geology*,
1164 *654*, 122060. https://doi.org/10.1016/j.chemgeo.2024.122060
1165 Vils, F., Müntener, O., Kalt, A., and Ludwig, T. (2011). Implications of the serpentine phase transition
1166 on the behaviour of beryllium and lithium-boron of subducted ultramafic rocks. *Geochimica et*
1167 *Cosmochimica Acta*, *75*(5), 1249–1271. https://doi.org/10.1016/j.gca.2010.12.007

Vitale Brovarone, A., and Herwartz, D. (2013). Timing of HP metamorphism in the Schistes Lustrés of Alpine Corsica: New Lu–Hf garnet and lawsonite ages. *Lithos*, *172–173*, 175–191. https://doi.org/10.1016/J.LITHOS.2013.03.009

Vitale Brovarone, A., Beltrando, M., Malavieille, J., Giuntoli, F., Tondella, E., Groppo, C., ... and Compagnoni, R. (2011). Inherited ocean–continent transition zones in deeply subducted terranes: insights from Alpine Corsica. *Lithos*, *124*(3-4), 273-290. https://doi.org/10.1016/j.lithos.2011.02.013

Vitale Brovarone, A., Beyssac, O., Malavieille, J., Molli, G., Beltrando, M., and Compagnoni, R. (2013). Stacking and metamorphism of continuous segments of subducted lithosphere in a high-pressure wedge: The example of Alpine Corsica (France). *Earth-Science Reviews*, *116*(1), 35–56. https://doi.org/10.1016/J.EARSCIREV.2012.10.003

Vitale Brovarone, A., Martinez, I., Elmaleh, A., Compagnoni, R., Chaduteau, C., Ferraris, C., and Esteve, I. (2017). Massive production of abiotic methane during subduction evidenced in metamorphosed ophicarbonates from the Italian Alps. *Nature Communications 2017 8:1*, *8*(1), 1–13. https://doi.org/10.1038/ncomms14134

Vitale Brovarone, A., Picatto, M., Beyssac, O., Lagabrielle, Y., and Castelli, D. (2014). The blueschist–eclogite transition in the Alpine chain: P–T paths and the role of slow-spreading extensional structures in the evolution of HP–LT mountain belts. *Tectonophysics*, *615*, 96-121. https://doi.org/10.1016/j.tecto.2014.01.001

Vitale Brovarone, A., Sverjensky, D. A., Piccoli, F., Ressico, F., Giovannelli, D., and Daniel, I. (2020). Subduction hides high-pressure sources of energy that may feed the deep subsurface biosphere. *Nature Communications*, *11*(1). https://doi.org/10.1038/s41467-020-17342-x

Wu, S., Wörner, G., Jochum, K. P., Stoll, B., Simon, K., & Kronz, A. (2019). The preparation and preliminary characterisation of three synthetic andesite reference glass materials (ARM-1, ARM-2, ARM-3) for in situ microanalysis. *Geostandards and Geoanalytical Research*, *43*(4), 567-584. https://doi.org/10.1111/ggr.12301

1194 Zhang, Y., Gazel, E., Gaetani, G. A., and Klein, F. (2021). Serpentinite-derived slab fluids control
1195 the oxidation state of the subarc mantle. In *Sci. Adv* (Vol. 7). DOI: 10.1126/sciadv.abj2515
1196

1197 ## Captions

1198 **Figure 1:** Geological map and interpretative cross section of the Monte Maggiore massif, modified after Jackson and
1199 Ohnenstetter (1981), Debret (2013), Basch *et al.* (2018), Fabbri *et al.* (2018), and the present study. The map colour codes
1200 refer to lithologies and, for ultramafic rocks, the degree of serpentinization. Open diamonds, squares, triangles, and circles
1201 refer to the nature of the protolith, while green, yellow, orange and blue refer to the characteristic serpentine assemblages
1202 described in Section 4.1.3.

1203

1204 **Figure 2. a)** Panoramic view of the Monte Maggiore massif, with interpreted geology. The regional foliation in the
1205 Centuri gneiss is shown by black dashed lines, with spacing marking the intensity of the deformation. Viewpoint position
1206 is reported in Fig. 1. **b, c, d)** Outcrop-scale pictures of the contact zone between the Monte Maggiore massif and the
1207 Centuri gneiss: massive serpentinite at about 20 m (b) and 5 m (c) above the contact and the contact zone with Centuri
1208 mylonite (d). Sampling spots marked with symbol "*". **e, f, g)** Photomicrographs of sample collected from the outcrops
1209 shown in panels b, c, and d. These rocks highlight the general absence of deformation in serpentinites from the basal
1210 portion of the Monte Maggiore body, and the strong strain localization inside the Centuri geniss, here represented by a
1211 Na-amphibole-Epidote-rich folded layer found inside the Centuri mylonite.

1212

1213 **Figure 3:** Interpretative, not-to-scale log of the Monte Maggiore serpentinization front, field features and petrographic
1214 images. **a-d**: Field images. **e-n**: photomicrographs under cross polarized light. **a**) Preserved peridotite crosscut by thin
1215 gabbro dykelets, with chlorite halo (black wall). The presence of Ca-Al minerals inside these structures, as well as the
1216 comparison with thicker equivalents, allowed us to infer their igneous origin. **b**) Partially serpentinized peridotite with
1217 oriented dark Liz/Atg veins. **c**) Deformed, partially serpentinized peridotite with a network of Atg2 veins and pyroxenes
1218 relicts. **d**) Massive serpentinite with altered pyroxenes. **e**) Liz vein network crosscut by Atg1 veins in preserved
1219 peridotite. Sample COR22-17. **f**) Partially serpentinized peridotite with Liz/Atg veins with associated metamorphic
1220 olivine (M-Ol) in the centre; Atg2 growing on the rims of Liz/Atg and at the expenses of primary olivine (P-Ol). Atg3
1221 growing at the expense of M-Ol and Liz/Atg. Sample COR21-79. **g**) Network of Atg2 veins in a deformed partially
1222 serpentinized peridotite, successively replaced by static Atg3 blades. Sample COR22-13. **h**) Massive serpentinite
1223 characterized by Liz/Atg veins replaced by static Atg3 blades. In the right corner of the image, closeup of Atg3

replacing primary clinopyroxene (P-Cpx) and a crosscutting Atg4 vein. Sample COR21-64l. Additional mineral abbreviations are defined in the text. Serp = serpentinized.

Figure 4.**a-b)** Images of partially serpentinized peridotites in cross-polarized light (a) and backscattered electron (BSE) (b). Note P-Opx rimmed by a corona of metamorphic clinopyroxene (M-Cpx) and former site of plagioclase (ex-Pl). Ex-Pl site is replaced by epidote (Ep) and chlorite (Chl). Sample Cor21-79. **c-d)** Photomicrographs of a partially serpentinized peridotite in cross polarized light (c) and BSE (d). P-Opx being is replaced by Atg2, M-Cpx, and M-Ol. The BSE image shows the presence of an inner corona of M-Cpx and a brighter rim of M-Ol. Note that M-Ol is brighter than P-Ol in BSE, indicating higher Fe contents in the former (see also Vitale Brovarone *et al.*, 2020). Sample Cor21-80 **e-f)** Photomicrographs of a serpentinite in cross polarized light (e) and BSE (f). P-Ol and P-Opx are completely replaced by Liz/Atg mixtures, M-Cpx and Mag are preserved along the cleavage of the ex-Opx. Sample Cor21-64f.

Figure 5: Backscattered electron images of serpentine microstructural features. **a)** Atg1 veins growing at the expense of Liz network. Sample COR21-30. **b)** Blades of Atg2 propagating through fractures in primary olivine. Sample COR21-51a (P-Ol). **c)** Liz/Atg veins network, with M-Ol growing in the center, Atg2 replacing P-Ol at the border of the veins and At3 replacing M-Ol. Cor21-79 **d)** Detail of Liz/Atg veins associated with metamorphic olivine (M-Ol) and magnetite (Mag), rimmed by Atg2 replacing P-Ol, and Atg3 replacing M-Ol. Sample Cor21-36. **e)** Detail of interface between P-Cpx replaced by Atg3 and former P-Ol replaced by a network of Liz/Atg associated with magnetite, partially substituted by Atg3. Sample Cor21-22f. **f)** Liz/Atg matrix in a serpentinite associated with Mag, crosscut by a fracture filled with Atg4 devoid of opaque minerals. COR21-22f.

Figure 6: Representative Raman spectra of the identified serpentine generations and metamorphic olivine. On the left low frequencies (200–1200 cm^{-1}), on the right OH stretching (3600 to 3750 cm^{-1}) ranges. Grey bands identify the characteristic bands for antigorite (373, 1044, 3670, 3700 cm^{-1}). Liz, Liz/Atg and M-Ol characteristic peak are reported next to the spectra.

Figure 7: Major element results and comparison with previous studies. **a**) Results of CIPW normalization (Kelemen *et al.*, 1992) for variably serpentinized samples in a ternary Ol, Opx, Cpx diagram. **b**) MgO/SiO2 vs. Al_2O_3/SiO_2 diagram; The Terrestrial Array should represent the initial composition of harzburgite and lherzolite for different elemental ratios (Jagoutz *et al.*, 1979; Hart and Zindler, 1986). **c**) MgO vs SiO_2 recalculated without LOI content. **d**) positive correlation between MgO/(MgO+FeO) and Fe_2O_3/Fe_{tot}.

Figure 8: Chondrite-normalized REE patterns (**a-f**), and primitive mantle-normalized selected trace element patterns (**g-n**) of serpentine minerals and M-Ol from preserved and partially serpentinized peridotites. Chondrite and primitive mantle values from Sun and McDonough (1989). Olivine composition from Basch *et al.* (2018), orthopyroxene and clinopyroxene composition from Rampone *et al.* (2008).

Figure 9: Chondrite-normalized REE patterns (**a-c**) and selected trace element patterns normalized to the primitive mantle (**d-f**) of serpentine minerals from serpentinites. Chondrite and primitive mantle values from Sun and McDonough (1989). Olivine composition from Basch *et al.* (2018), orthopyroxene and clinopyroxene composition form Rampone et al (2008).

Figure 10: Concentrations of Li, B, Sr, Cs, Ba, Rb, Pb, and U in the serpentine generations recognized, subdivided into preserved-partially serpentinized peridotites (0 - 75 vol. % serp.) and serpentinites (75 - 100 vol. % serp.). Boxplot colours refer to each generation. Number in parentheses indicates the number of analyses for each generation, including analyses bdl which cannot be represented in this graph.

Figure 11: Potential serpentine evolution models of Monte Maggiore massif (MM). Generic P-T path geometries are from Syracuse *et al.*, 2010 and Holt and Condit (2021). **a**) Serpentine mineralogical evolution of Monte Maggiore explained by prograde heating during subduction (Schwartz *et al.*, 2013). **b**) Serpentine mineralogical evolution of Monte Maggiore explained by silica addition, favouring the formation of antigorite relative to lizardite at lower T. **c**) Serpentine mineralogical evolution explained by evolving subduction zone thermal gradients with subduction maturity (Holt and Condit, 2021). The latter hypothesis would result in opposite serpentine polysome chronology (antigorite to lizardite) than that observed here, and it is therefore discarded (see text for details).

Figure 12: Bar plots and median value showing *in situ* Li, B, Sr, and Ba concentrations for Monte Maggiore (this study), Semail ophiolite (Prigent *et al.*, 2018) and Lanzo Massif (Debret *et al.*, 2013b) serpentinites across serpentinization fronts. The dataset of each locality is subdivided in two groups referring to the relative distance of the samples from the tectonic contact. For Monte Maggiore and Lanzo, the serpentinization degree was taken in account to distinguish the two classes and is reported at the bottom of each bar plot. The number of analyses for each bar is reported on top. For the Semail ophiolite, each analysis refers, as reported by Prigent *et al.* (2018), to a mean of multiple analyses, therefore the median value is not reported.

Figure 13: Models of FME distributions across serpentinization fronts in the different settings. **a**) Sketch of subduction zone system (modified after Zhang *et al.*, 2021) illustrating the environments of hydration and dehydration of the considered localities. SO: Semail Ophiolite, MM: Monte Maggiore massif, ET: Erro-Tobbio massif, Lz: Lanzo. **b**) Close-up of the MM case study, interpreted here as a slice of subducted oceanic mantle coupled to the overlying mantle wedge and overlying the Alpine slab. See also Scambelluri and Tonarini (2012) for a similar reconstruction for the Erro-Tobbio massif, Western Alps. **c**) Interpretative sketches summarizing the origin of fluids involved in the serpentinization fronts in, from left to right, the Semail ophiolite, Monte Maggiore massif, and Lanzo. The Semail ophiolite and the Monte Maggiore massif were infiltrated by metamorphic fluids, resulting in an enrichment of FME at the base of the serpentinization front, as discussed here. The Lanzo massif profile may instead represent the result of dehydration and/or deformation (Debret *et al.*, 2013b) or inherited oceanic serpentinization patterns.

Figure 1

Click here to access/download;Figure;Fig.1.jpg

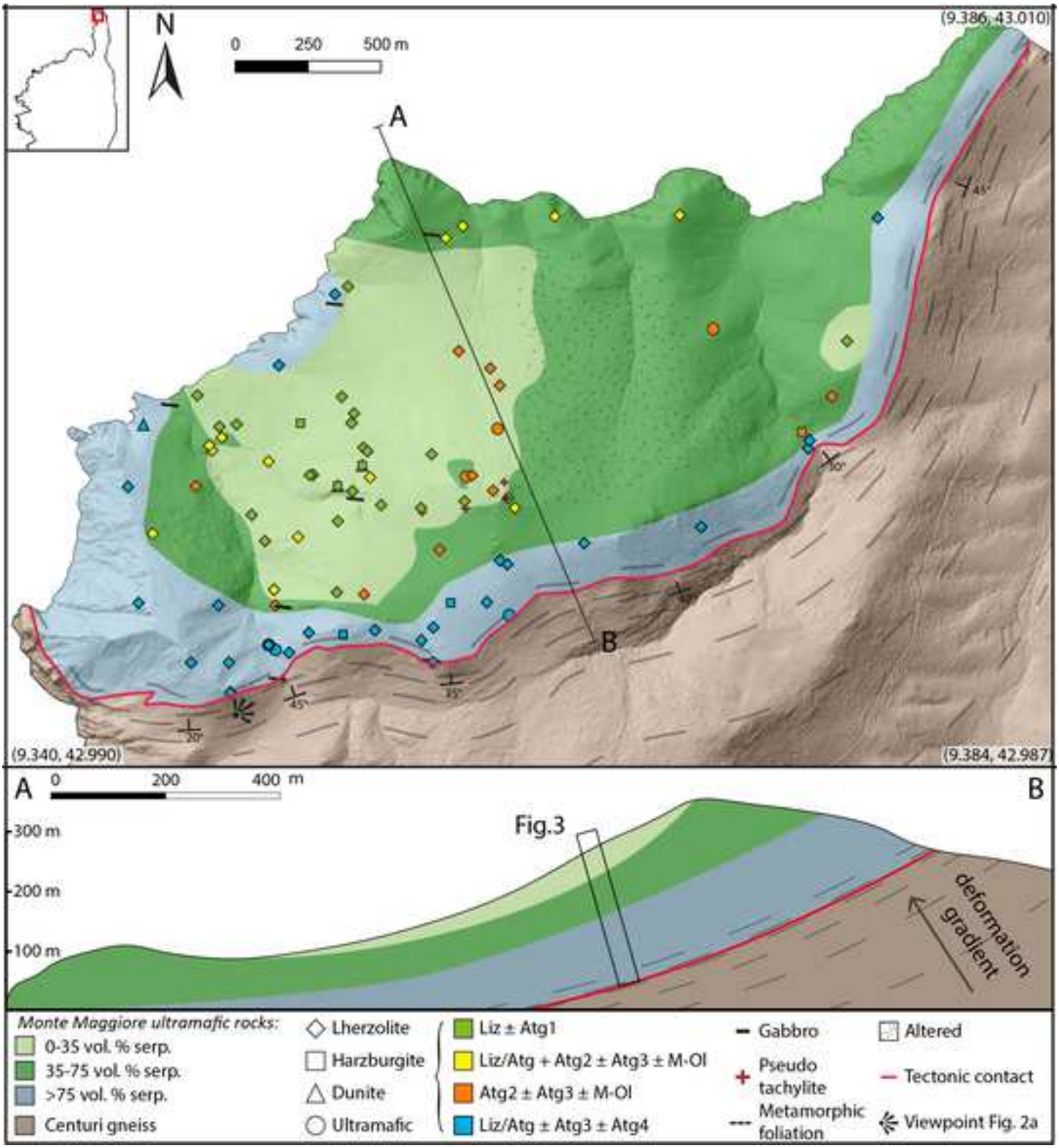

Figure 2

Click here to access/download;Figure;Fig.2.jpg

Figure 3

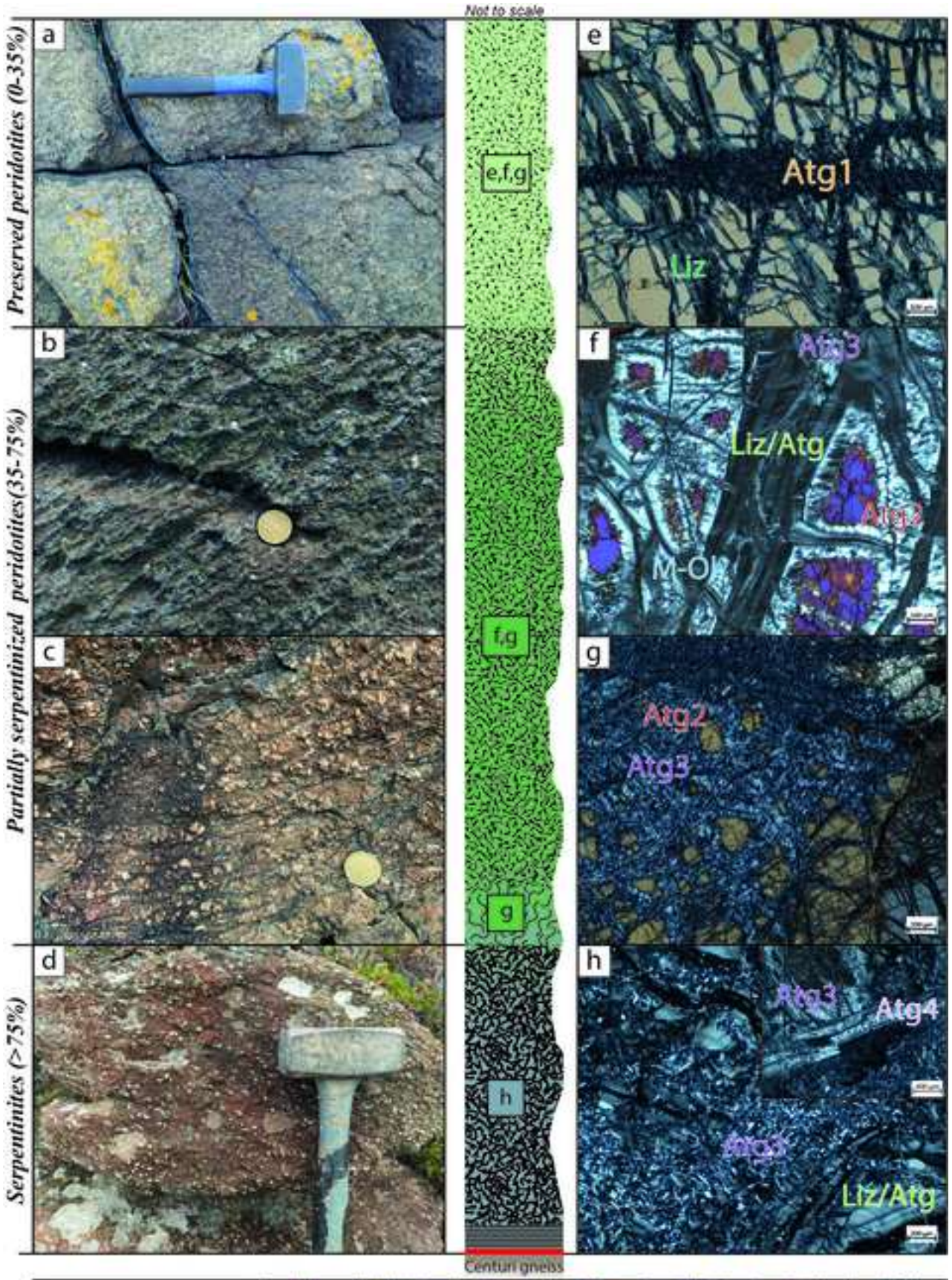

	Liz	Liz/Atg	Atg1	Atg2	Atg3	Atg4	M-Ol
Preserved peridotites	▬	-	▬	-			-
Partially serp. peridotites	-	▬	-	▬	▬		▬
Serpentinites		▬			▬	-	

deformed serp. peridotites | foliated serpentinites | tectonic contact | abundance: - rare ▬ common

Figure 4

Click here to access/download;Figure;Fig.4.tif

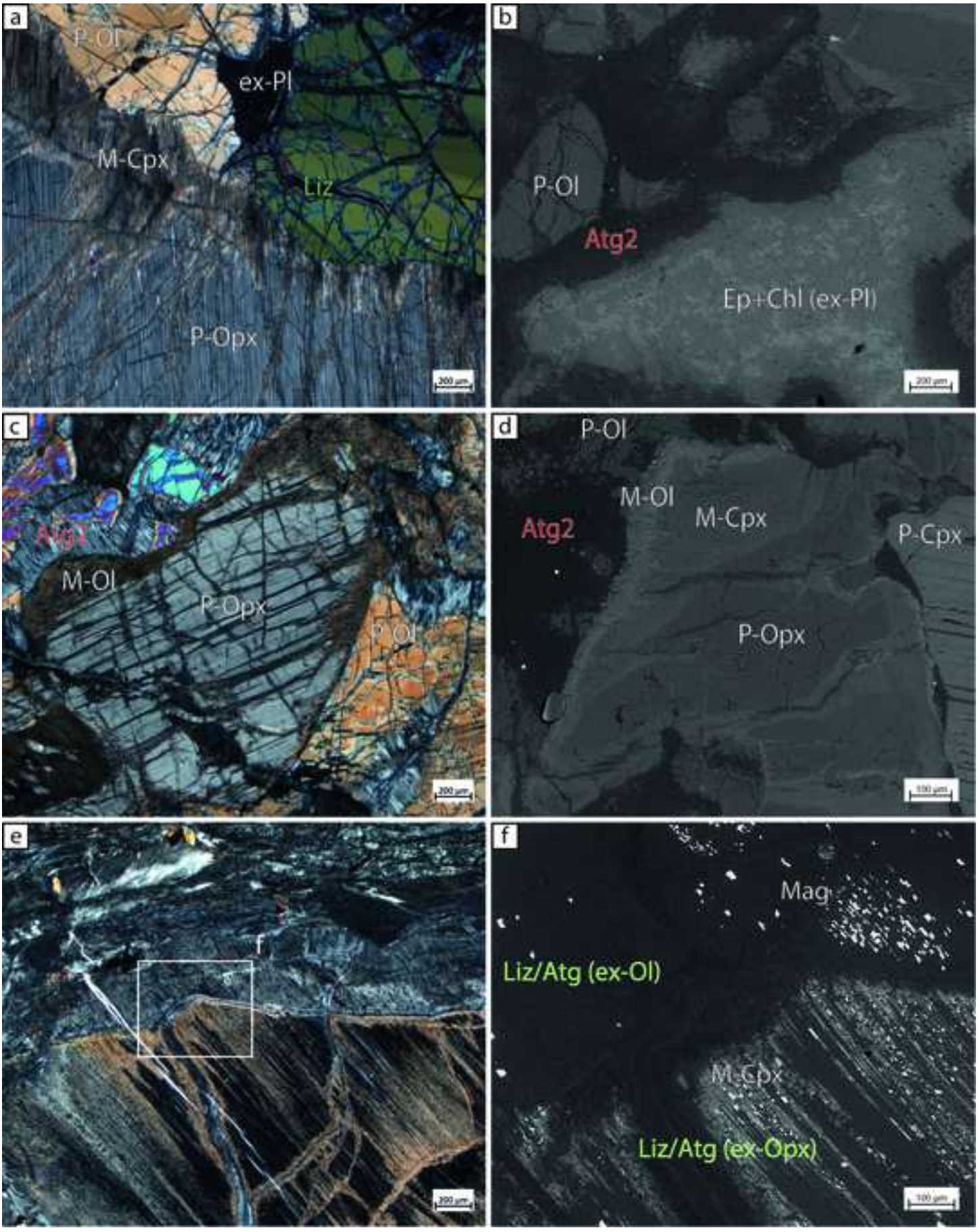

Figure 5

Click here to access/download;Figure;Fig.5.tif

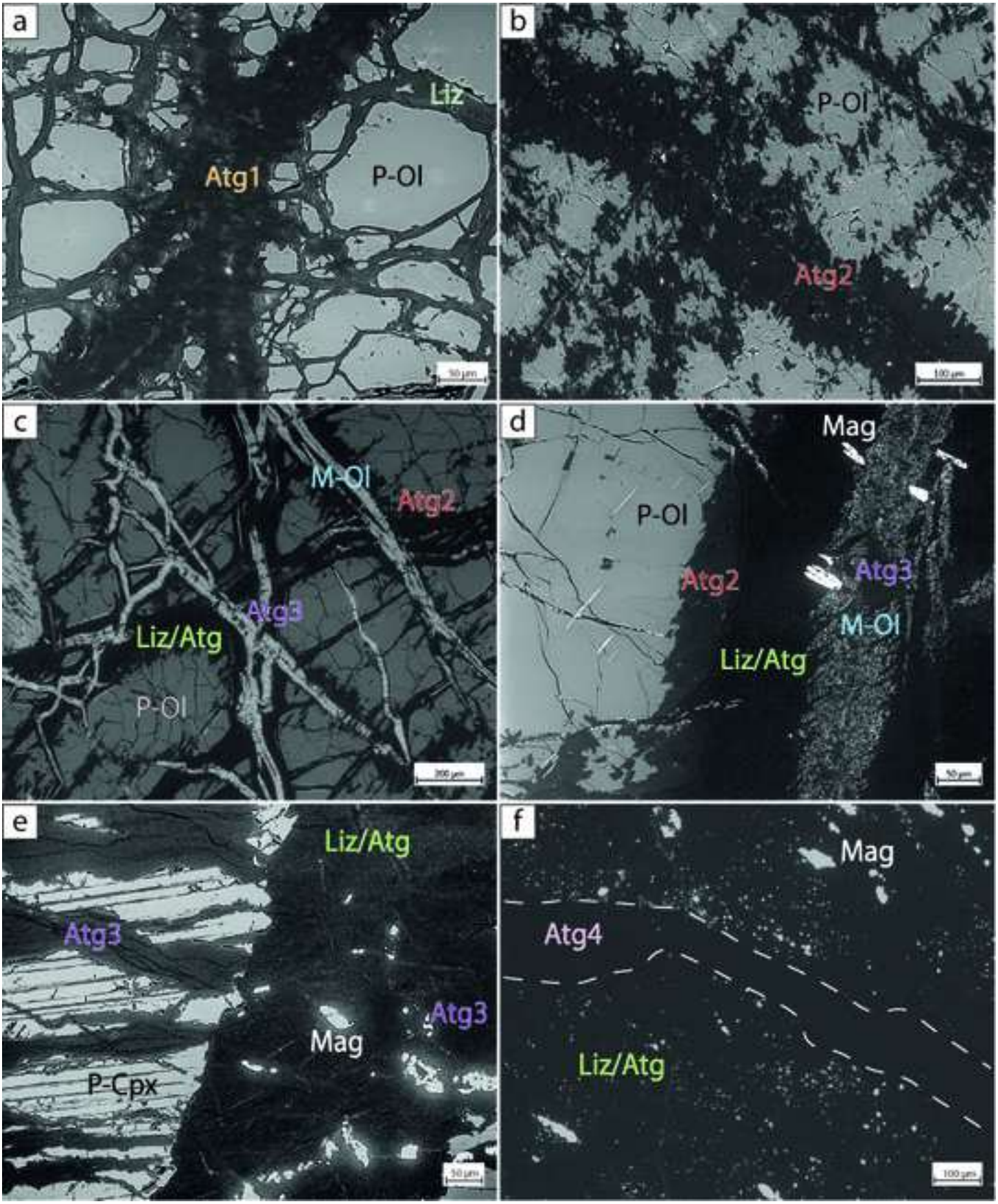

Figure 6

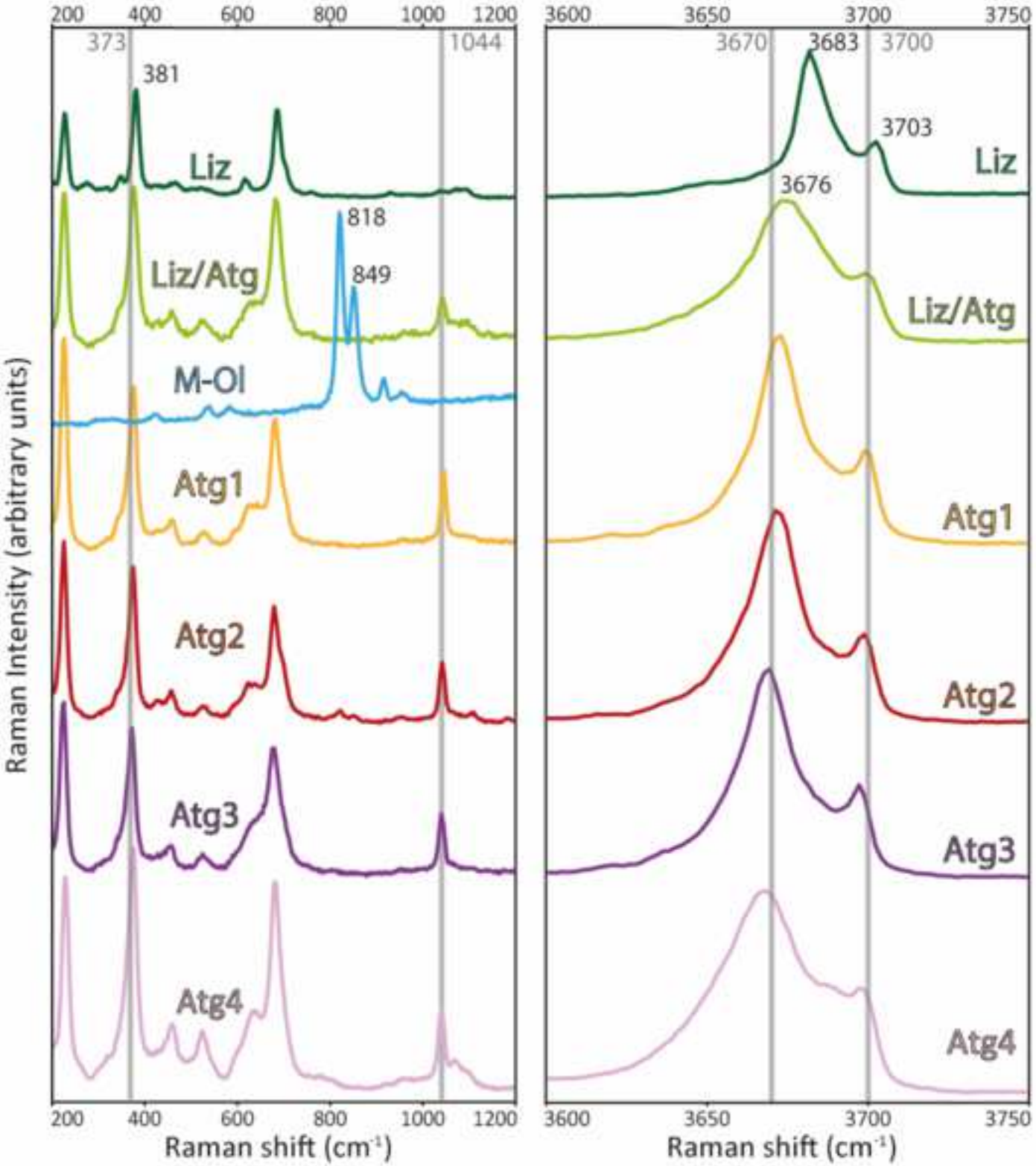

Figure 7

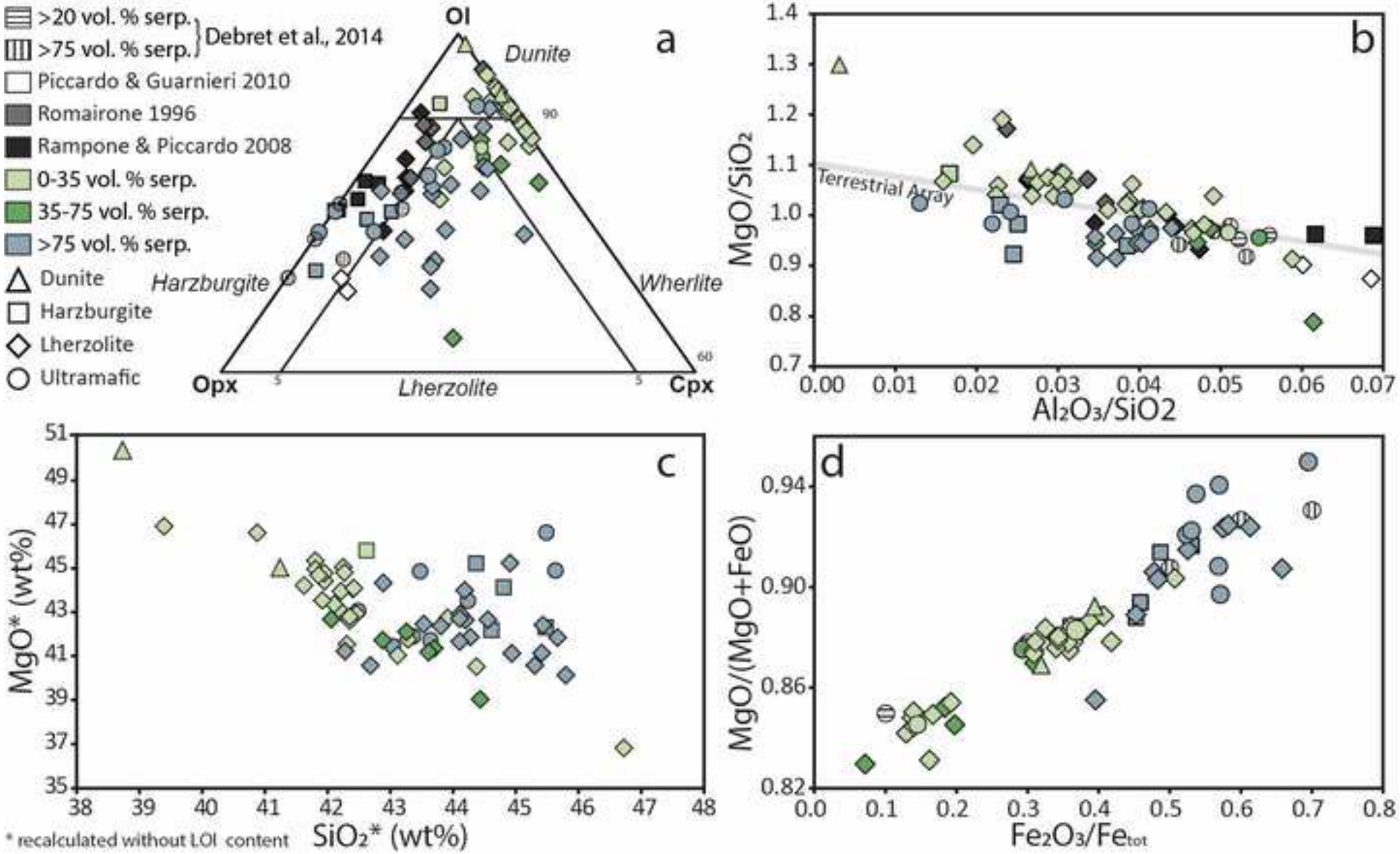

Figure 8

Click here to access/download;Figure;Fig.8.jpg

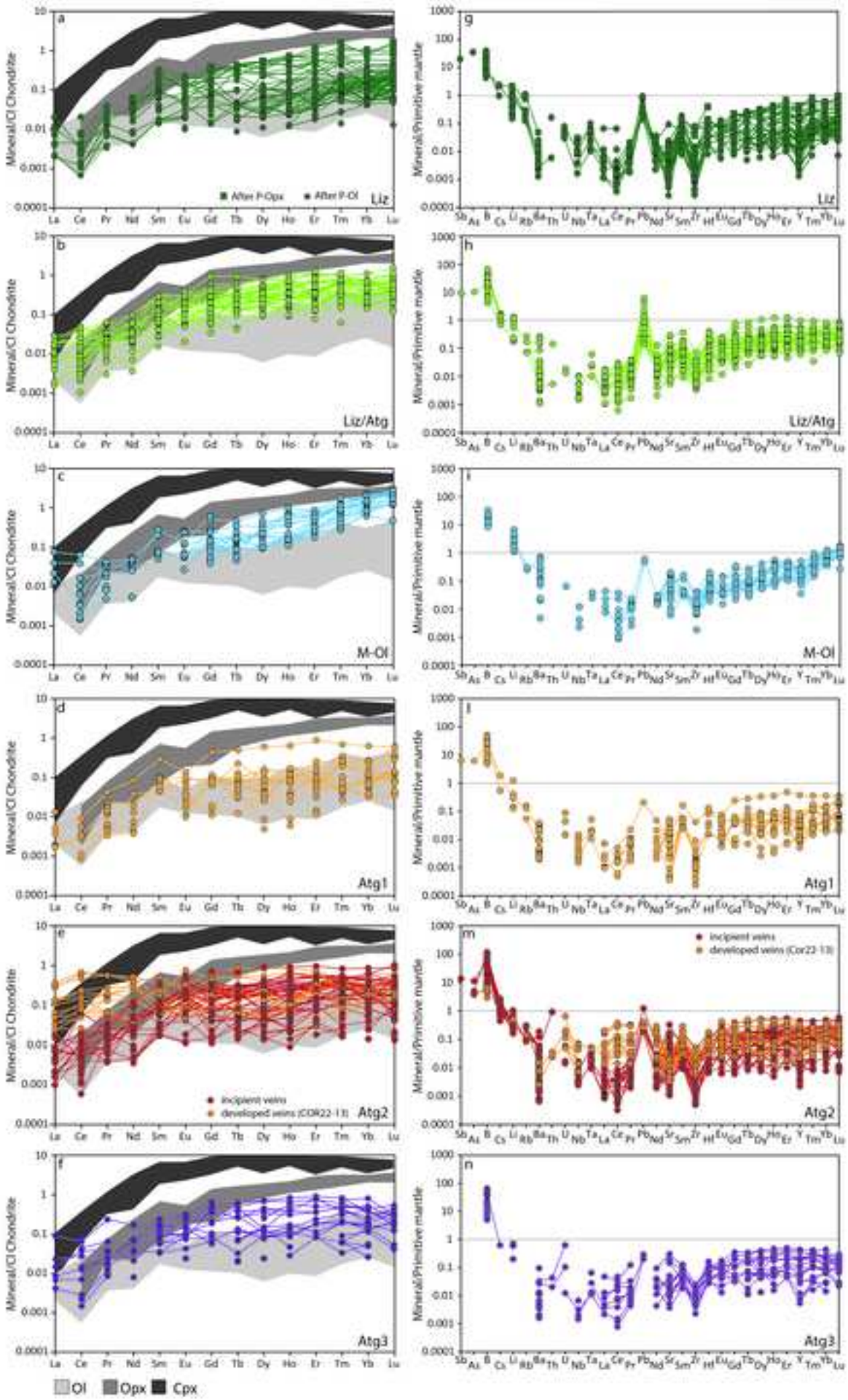

Figure 9

Click here to access/download;Figure;Fig.9.jpg

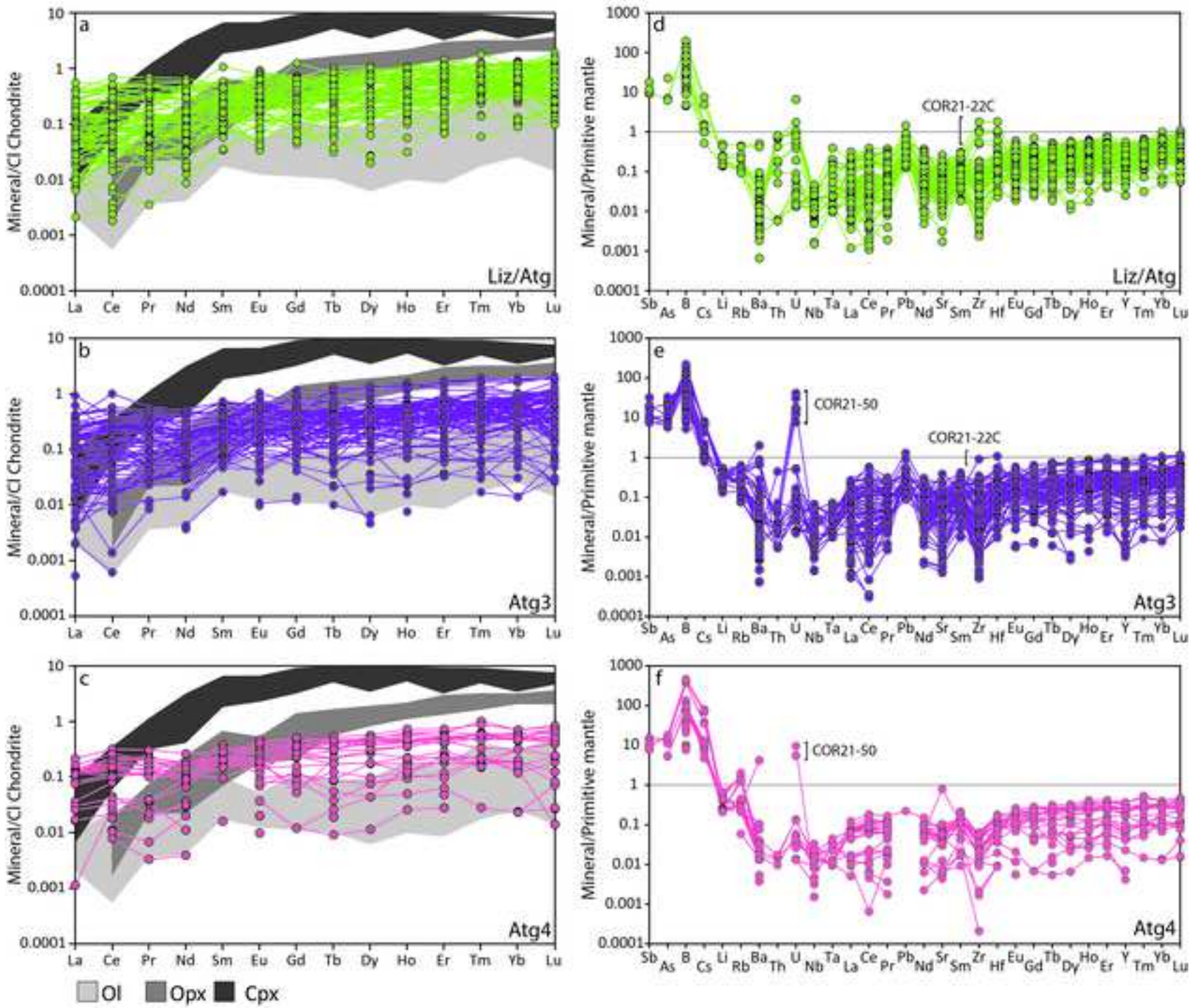

Figure 10

Click here to access/download;Figure;Fig.10.jpg

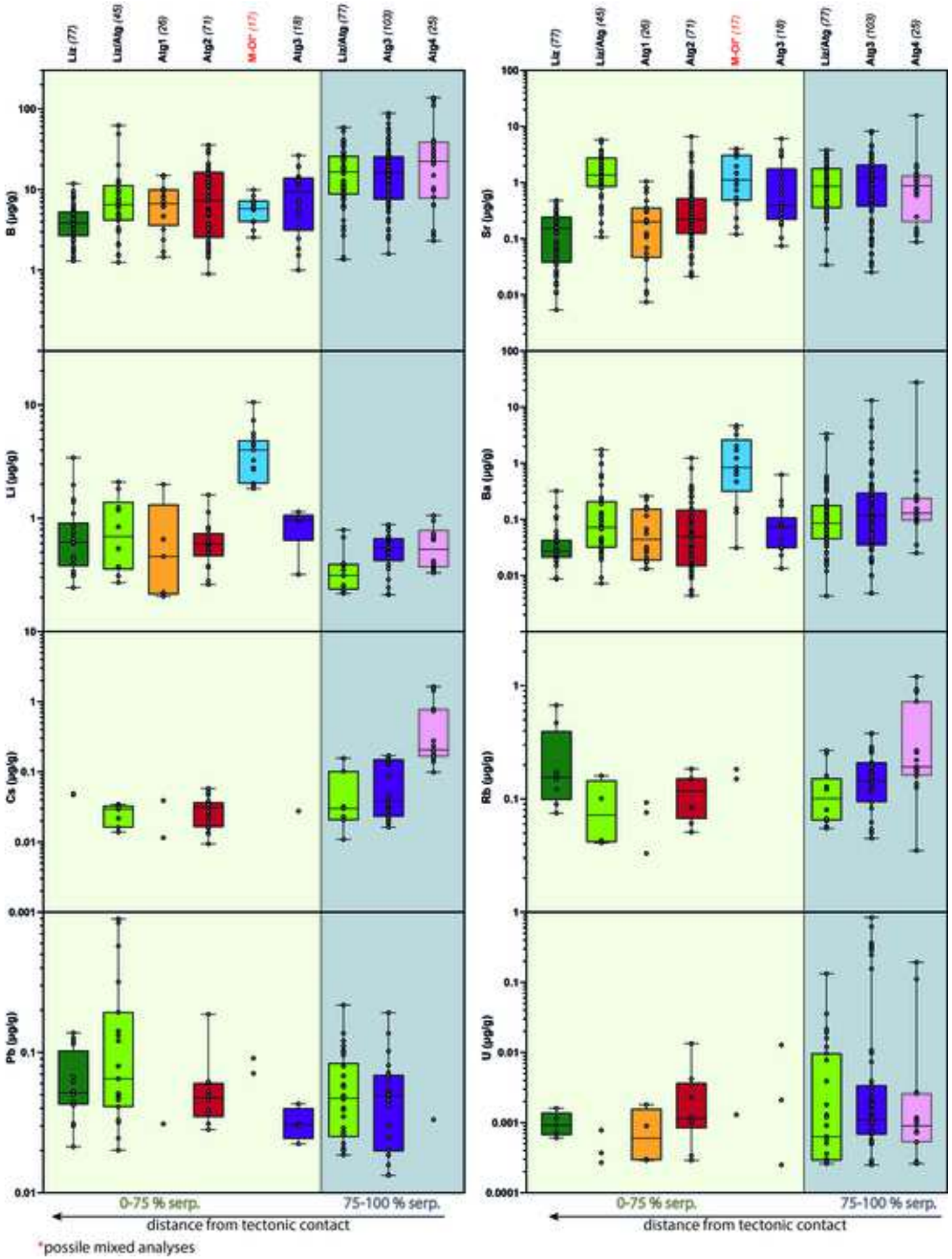

Figure 11

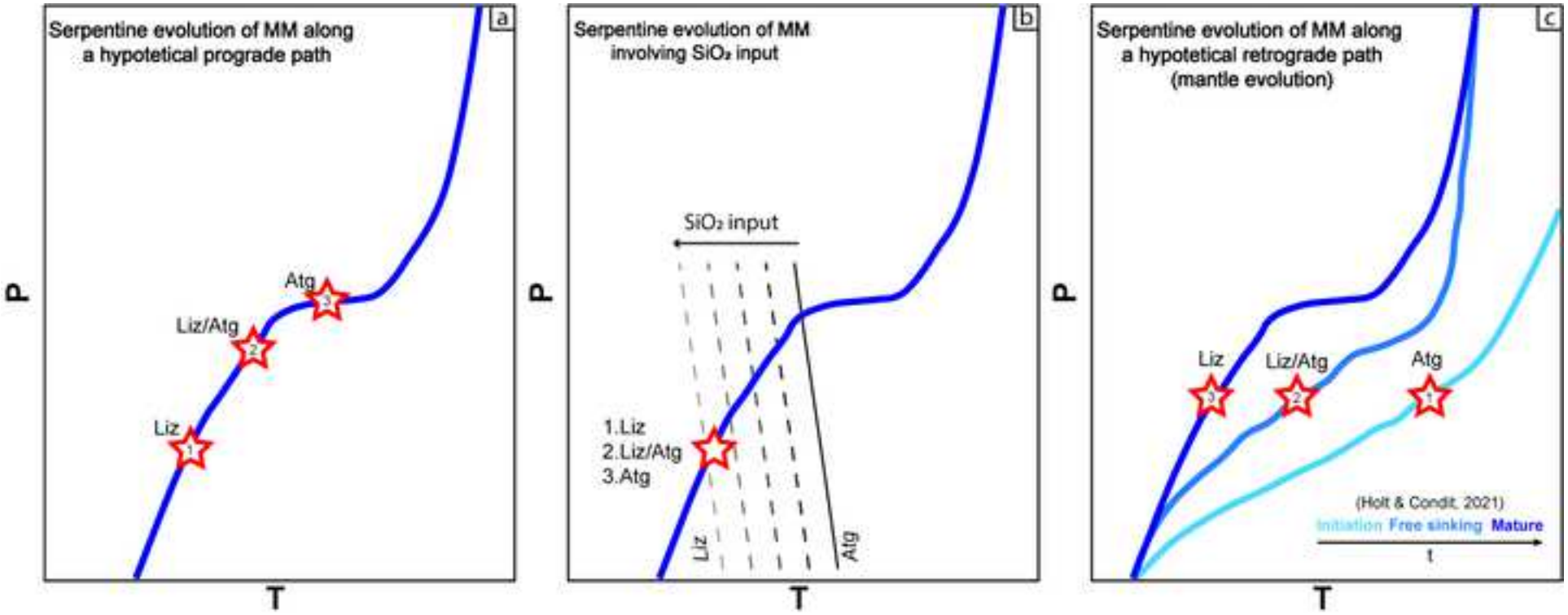

Figure 12

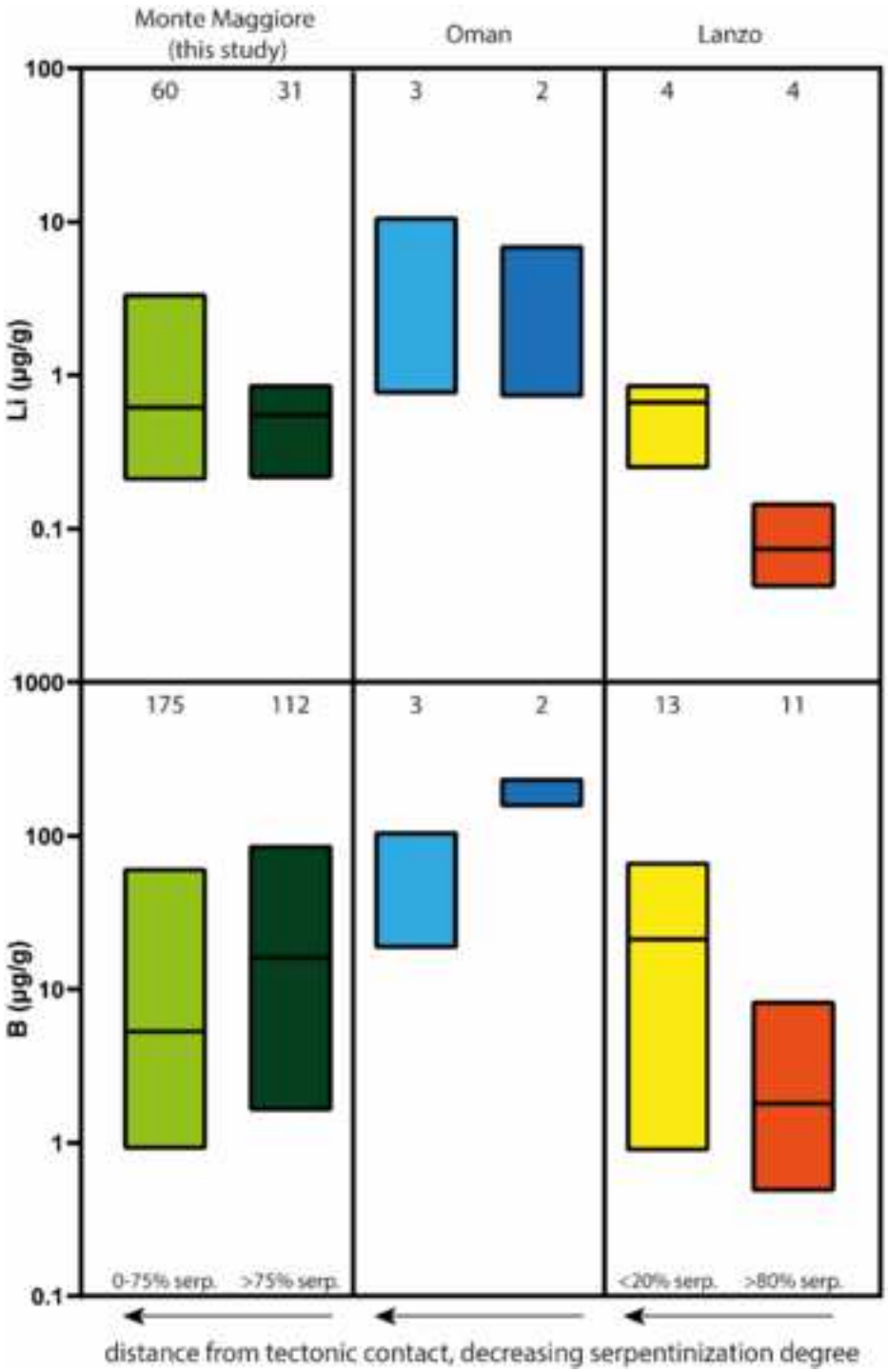

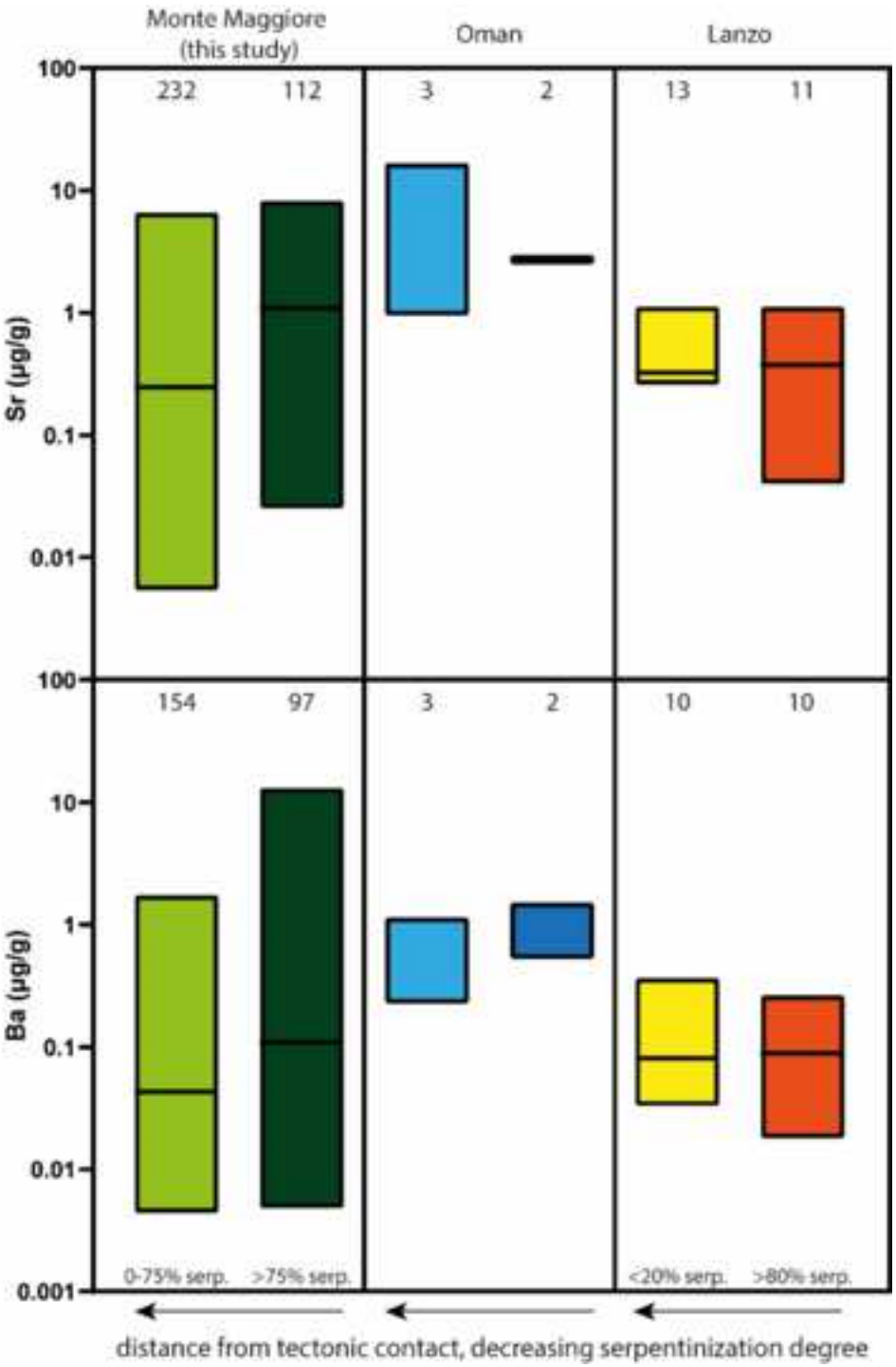

Figure 13

Click here to access/download;Figure;Fig.13.jpg